

Single-ion irradiation: physics, technology and applications

This article has been downloaded from IOPscience. Please scroll down to see the full text article.

2008 J. Phys. D: Appl. Phys. 41 043001

(<http://iopscience.iop.org/0022-3727/41/4/043001>)

The Table of Contents and more related content is available

Download details:

IP Address: 91.202.128.88

The article was downloaded on 03/11/2008 at 11:15

Please note that terms and conditions apply.

TOPICAL REVIEW

Single-ion irradiation: physics, technology and applications

Iwao Ohdomari

Faculty of Science and Engineering, Institute for Nanoscience and Nanotechnology, Waseda University, Tokyo, Japan

Received 1 August 2007, in final form 19 October 2007

Published 28 January 2008

Online at stacks.iop.org/JPhysD/41/043001**Abstract**

Among the various radiation effects which involve the study of radiation environments, responses of materials and devices to radiation, radiation testing and radiation hardening of devices and equipment, this review mainly considers the radiation effects induced by alpha particles and other ions used in semiconductor technology on Si crystals and Si devices.

We first describe the single-ion microprobe that enables the study of the site dependence of radiation hardness in a semiconductor device. Next, we describe single-ion implantation as a tool for suppressing fluctuation in device function induced by the discrete number and random position of dopant atoms. Finally, we describe the common features associated with both ‘probing’ and ‘modification’ in terms of the nature and behaviour of defect clusters induced by single-ion irradiation.

A special feature of the review is that the radiation effects discussed here are induced by ‘single’ particles, and not by particle beams. Although there is a great amount of accumulated data on radiation effects, they are discussed in the conventional terms of ‘dose’ or ‘fluence,’ whose unit is cm^{-2} . Therefore, this review provides complementary information on radiation effects.

(Some figures in this article are in colour only in the electronic version)

1. Introduction

Over the years, research on radiation effects has involved the study of radiation physics, radiation environments, responses of materials and devices to radiation, computer simulation for particle transport, radiation testing and radiation hardening of devices and equipment. A comprehensive survey of these studies has been compiled into a handbook [1] that provides an overview of all aspects of radiation effects. The handbook appropriately discusses the radiation effects of gamma and x rays, alpha particles, electrons, positrons, neutrons and protons on devices and systems such as MOS devices, bipolar transistors and integrated circuits, diodes, solar cells and optoelectronics, power semiconductors, microelectronics, sensors, MEMs and other components.

This review mainly considers the radiation effects induced by protons, alpha particles and other ions used in semiconductor technology on Si crystals and Si devices. A

special feature of the review is that the radiation effects discussed herein are induced by ‘single’ particles, and not by particle beams. This is in contrast to the previously mentioned handbook, where all data are discussed in the conventional terms of ‘dose’ or ‘fluence,’ whose unit is cm^{-2} . In conjunction with the handbook, we believe that this review will therefore provide complementary information on radiation effects.

With regard to the events induced in a device by a single particle, there exists a paper on soft failures in computer electronics by ‘single radioactive atom decay’ [2]. For example, it is reported that a DRAM memory chip is hit by approximately one radioactive fragment per minute and a single alpha particle can cause four memory cells to change their content from a one to a zero. In this regard, the concepts of soft failures and ‘funnelling’ induced by single particles are pioneering. However, this paper primarily focuses on IBM’s efforts to pinpoint sources of radioactive contamination from various environments and materials used in their processes. In

Table 1. Chronology of researches on single-ion irradiation.	
1960s	Advent of Rutherford backscattering spectroscopy (RBS).
1980s	Advent of ion microprobe (IMP) technology.
1992	Development of single-ion microprobe (SIMP) at Waseda University.
1992	Application of SIMP to mapping site dependence of single-event upset (SEU) or ‘soft-error’ hardness in semiconductor devices.
1994	Development of single-ion-induced charge (SIBIC) imaging using SIMP for high-precision mapping of radiation immunity in fine semiconductor devices.
1994	Application of SIMP to test total dose effects.
1994	Proposal of single-ion implantation (SII) by Ohdomari.
1996	Application of SIMP to diagnosis of devices such as MOSFETs, p–n junctions and Schottky diodes.
1996	Development of first SII machine.
1997	Analysis of radiation-induced defects at SiO_2/Si interfaces using SIMP.
2000	Proposal for National Nanotechnology Initiative by US President Bill Clinton.
2000	Success in ‘trimming’ conductance value of fine semiconductor resistors using SII for smaller fluctuation.
2001	Development of ion-gun/high-temperature scanning-tunnelling-microscope (STM) combined system (IG/STM) and success in <i>in situ</i> observation of vacancy cluster behaviour in Si.
2005	Creation of a novel semiconductor with an ordered dopant array using SII.
2005	Success in <i>in situ</i> observation of Si interstitial behaviour using IG/STM.
2005	Development of a liquid-metal-ion-source (LMIS) ion-gun/high-temperature STM combined system (LMIS-IG/STM).

addition, approaches to radiation hardening considered whole chips and statistically processed data, although the events themselves are induced by single particles. As discussed later in the text, our approach to device diagnosis is based on the pinpoint irradiation of a fine semiconductor device area with single particles. In this aspect also our work complements previous and traditional studies.

2. History of researches on single-ion irradiation (SIIr)

A chronological list of researches on SIIr is presented in table 1.

Ion implantation (I/I) technology has played an essential role in the astounding growth of Si ultra-large-scale-integration (ULSI) technology through device size reduction. The technology capitalizes on the straight paths of ions when they penetrate a device structure. Until I/I had developed into a doping technology, it was necessary to extensively study various I/I phenomena such as ion and disorder distributions in a target, the annealing of disorders and lattice sites of implanted ions, and their influence on electrical properties. Rutherford backscattering spectroscopy (RBS), developed in

the 1960s, is a very powerful non-destructive tool to ‘probe’ ion implantation phenomena by utilizing the very small scattering cross section characteristic of the high energies of the probe ions.

As the application of electronic devices expanded into many new and sometimes hostile environments such as space or areas close to nuclear reactors [3, 4], the industry became concerned about the possible degradation and decreased reliability of devices due to radiation effects on their small feature size. Consequently, the topic of radiation hardness attracted considerable interest in the field of electronics.

Device structures must be optimized for improved radiation hardness on the basis of information obtained from radiation effects in local device areas. In the 1980s, ion microprobe systems (IMPs) evolved from the RBS. They were characterized by a collimated high-energy ion beam with a diameter of sub-micrometres to a few micrometres, and they served as a good tool both for irradiation and analysis of a localized area on a target [5]. IMPs also played an important role in mapping the elemental distribution in a target and obtaining three-dimensional information on the elemental distribution by combining their areal resolution with the inherent depth resolution of the RBS. The expansion of IMP applications demanded an increasing ion current in order to obtain better statistics. However, extremely high-current densities posed a serious problem because of the radiation damage they caused to a specimen. Even though a beam scanning system was used to reduce such radiation damage [6], there still remained the problem of beam induced effects; for example, an extremely high ion dose over a relatively small area could easily lead to specimens being destroyed completely.

The tandem accelerator used for the IMP at Waseda University [7, 8] was found to be unsuitable for increasing the ion current intensity; therefore, we decided to use the opposite approach, namely, reduce the ion current drastically and isolate the ions from the ion beam. The first single-ion microprobe (SIMP) was invented in 1992 [9, 10]. The SIMP proved to be very powerful to test the radiation hardness of semiconductor devices with a feature size of a few micrometres for space applications. However, an even greater advantage of the SIMP was that it enabled the study of the site dependence of the radiation hardness in a semiconductor device. It was first applied to test the so-called single-event upset (SEU) or ‘soft-error’ hardness of semiconductor devices [9–13]. The SIMP was also applied to imaging device features [14] before testing the site-dependent radiation hardness [13, 14]; testing total dose effects [15, 16] and radiation immunity of MOSFETs [17, 18], p–n junctions [19, 20] and Schottky diodes [21, 22]; and analysing radiation-induced defects at SiO_2/Si interfaces [23–25].

In the mid-1990s, semiconductor sizes were reduced in conformance with Moore’s law [26], which states that the number of components per chip doubles every 24 months. This reduction was beyond the ability of the SIMP to analyse because of its insufficient areal resolution. In the course of our study to seek better areal resolution for single-ion technology, we found that in the era of nanometre-size devices,

the distance between dopant atoms is comparable to the device size. Moreover, fluctuation in device functions due to that in the dopant number is not negligible anymore. So finally in 1994, we decided to develop single-ion implantation (SII) as a tool to suppress the fluctuation in device function induced by that in the discrete dopant number [27]. The first SI implanter was developed in 1996 by adding new features to an existing focused ion beam (FIB) system. These new features included extraction of single ions [28, 29], singularity of extracted ions [29], detection of single-ion incidence [29–33] and high aiming precision [34]. By improving these technological factors sequentially, we were finally able to control the number and position of the dopant ions [35–37].

In the late 1990s, the minimum feature size of Si ULSI devices was reduced to less than 100 nm. In addition, in February 2000, the then US President Bill Clinton submitted a bill to propose the National Nanotechnology Initiative (NNI). This bill triggered worldwide competition in nanotechnology. We intended to develop nanotechnology that was practical in terms of the process time, throughput and cost and decided to capitalize on ion irradiation for nanometre-scale surface modification of solids and subsequent wafer-scale wet processing. Since the modification of materials with ions was inevitably accompanied by the formation of disorders in the specimens, we initiated work on the behaviour of point defects and their complexes in Si [38], even while SII development was ongoing. One such task was to directly ‘see’ the solid surfaces before, during and after ion irradiation. For this purpose, we developed an ion-gun/high-temperature STM combined system (IG/STM) [39, 40]. Very recently, we added a new feature to the IG/STM: a liquid metal ion source (LMIS) for impurity doping, i.e. we developed an LMIS-IG/STM combined system [41].

This review consists of five sections. In section 3, we describe the SIMP as a tool for probing Si device functions and in section 4, we describe the SII as a tool for modifying material properties on the nanometre scale. In section 5, we describe the common features for both probing and modification, namely, the fundamental aspects of phenomena associated with SIIr. In section 6, we describe the future prospects of SIIr as concluding remarks.

3. Single-ion microprobe (SIMP)

3.1. Introduction—advantage of SIIr

There are three advantages of using SIIr as a tool to probe device functions or modify solid surfaces.

First, SIIr is the only direct tool to study SEUs that occur in microelectronic circuits. An SEU or a soft error is a change in state caused by high-energy particle collision at a sensitive node in a microelectronic circuit. An SEU itself does not permanently damage circuit functionality. However, in prevailing CMOS circuits because of low power consumption, the ‘parasitic’ thyristor inherent in CMOS structures can cause an apparent short circuit from power to ground. This condition is referred to as latch-up and it could destroy a device by thermal runaway. SEU was one of the most serious

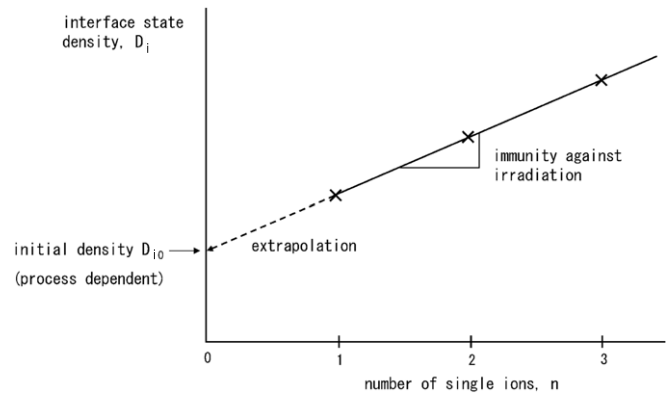


Figure 1. Application of SIIr, e.g. diagnosis of interfaces in a device. The gradient shows the immunity of the interface against ion irradiation. Extrapolation to zero ions yields the original function value, which may be below the detection limit in other methods.

problems in realizing highly reliable spacecraft electronics systems for long space missions. However, its mechanism was not fully understood on the microscopic scale. SEU phenomena depend not only on the colliding particle species but also on the collision sites on the microcircuits. To observe the transient charge pulses from an SEU, a single particle must exactly collide at the desired site on the microcircuit. Such an experiment should fulfil the following three technical requirements: (1) the micro beam spot size should be $1\text{ }\mu\text{m}$ or smaller, (2) the beam positioning accuracy should be within $\pm 1\text{ }\mu\text{m}$ and (3) single-ion collision should occur [11]. Our SIMP with a beam size of $2\text{ }\mu\text{m}$ was capable of single-ion collision and therefore reasonably fulfilled these requirements. In terms of available ion species and acceleration energy, SIMP is useful for resolving the soft error in memory devices, an SEU phenomenon induced by alpha particles in the energy range of a few million electronvolt. The rather poor areal resolution of the SIMP was not harmful for space applications of semiconductor devices, because the feature size of the devices need not be so small for high radiation hardness. Examples of the intense demand for much higher resolutions will be discussed in the next section.

Second, SIIr needs to be a low-dose process to minimize side effects due to radiation damage. This is very important because to test the immunity of devices, we must visualize and find beforehand collision sites for single particles. The direct and most accurate way to visualize is to use secondary electrons or electronic charges induced upon ion incidence; however, this process might inevitably result in radiation damage. This might obscure the SEU phenomena themselves. Therefore, the cost of visualizing device features must be minimized [14].

Third, SIIr enables more quantitative device diagnosis [27]. For example, in the case of an interface, by capitalising on the high controllability of the number of ions, a known amount of interface states, D_i , could be induced at the interface as a function of the number of ions, n . The correlation, D_i versus n , should be characteristic of the immunity of a particular interface to ion irradiation, as schematically shown in figure 1 [27]. The value, dD_i/dn , would be high for ‘fragile’ interfaces. Extrapolation of the D_i versus n curve to zero ions would

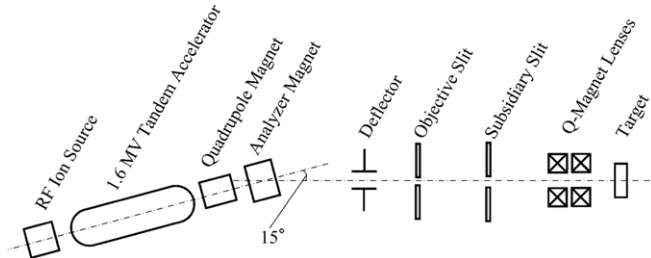


Figure 2. Experimental setup of the single-ion microprobe system (SIMP) at Waseda University.

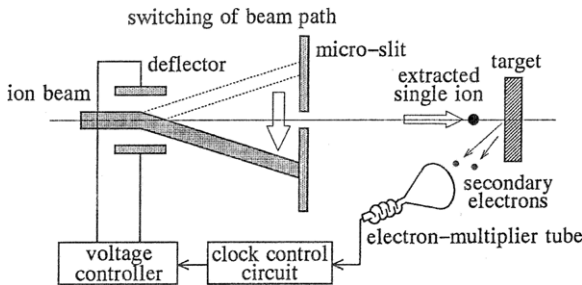


Figure 3. Principle of single-ion extraction.

enable us to estimate the initial interface state density D_{i_0} , which may not necessarily be measurable because of too low a density. A quantitative analysis of D_{i_0} as a function of the process parameters would give us more detailed information on process integrity.

3.2. Setup of SIMP

Figure 2 shows the experimental setup of the SIMP. The beam line, which consists of objective slits, subsidiary slits, a lens system, scanning deflectors and a target chamber, was connected to a tandem accelerator (NEC 5SDH) with a terminal voltage of 1.6 MV [7, 14]. The lens system was a Heidelberg-type magnetic quadrupole doublet [42]. To the target chamber we added a scanning electron microscope (SEM) column, annular type solid-state detector (SSD) for RBS, Si(Li) x-ray detector for particle-induced x-ray emission (PIXE) and electron multiplier tube.

As shown in figure 3, each single-ion was extracted from the ion beam by ‘chopping’. Chopping is the operation of switching the ion beam to extract ions. An ion beam blocked by an aperture by applying a bias to a beam chopping deflector is switched to the opposite side of the aperture by applying a reverse bias to the deflector and is blocked again by the aperture. Just at this moment, a very small number of ions can pass through the aperture. The extracted ions are focused with the high-precision quadrupole magnet and irradiated within an area corresponding to a beam spot size of about $2 \times 2 \mu\text{m}^2$ (FWHM). The number of extracted ions is counted using an electron multiplier tube by detecting secondary electrons emitted upon ion incidence. Signals from the electron multiplier tube are fed to the chopper controller, which keeps on sending the beam chopping signal to the deflector until the desired number of single ions are extracted.

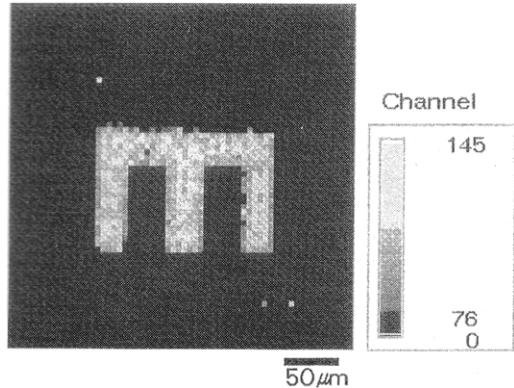


Figure 4. SIBIC image of the drain area in a test device. The scanned area is $128 \times 128 \mu\text{m}^2$.

The singularity and controllability of the number of extracted ions are confirmed beforehand by counting the number of etch pits formed in a high-sensitivity ion detector (CR-39) [31].

For device diagnosis, a particular site in the device must be aligned with the ion beam. Ion-beam-induced current imaging (IBIC) is advantageous for imaging ‘device features’ directly by using ion-beam induced charges at a p–n junction or a Schottky junction, and it is achieved by combining it with an IMP technique [43]. In IBIC imaging, the transient current is used intelligently to image a localized active area in micron-size devices. Energetic ion irradiation, however, induces crystal defects in semiconductor substrates, reduces the amount of charges induced by ion irradiation and lowers the charge pulse height. Angel *et al.* showed that a 2.0 MeV He⁺ beam at a dose of $2400 \text{ ions } \mu\text{m}^{-2}$ obviously damaged an Si p–n junction diode and reduced pulse heights [44]. Breese *et al* concluded that the ion-induced pulse height could be detected in an IBIC pulse height spectrum for a DRAM at the lowest dose of about $100 \text{ protons } \mu\text{m}^{-2}$. Above the critical dose, pulse height lowering by ion-induced damage degraded the IBIC image contrast drastically and made subsequent diagnosis impossible. Thus for IBIC imaging, the ion dose must be reduced to as low a level as possible. Figure 4 [14] shows an IBIC image obtained with our SIMP (single-ion-induced charge (SIBIC) image). This image is of the drain area of a commercial CMOS IC obtained at an ion dose of $0.2 \text{ ions } \mu\text{m}^{-2}$, which corresponds to only five ions per $5 \times 5 \mu\text{m}^2$ pixel. The image is composed of 64×64 pixels and corresponds to $320 \times 320 \mu\text{m}^2$ with a step width of $5 \mu\text{m}$. The image clearly reveals the shape of the drain region and its quality is good enough for the purpose of sample positioning. Figure 5 [14] shows the average charge pulse height as a function of the ion dose directed onto the central area of the drain. The average charge pulse height starts to decrease at a dose higher than 3000 ions, as indicated by the arrow. For the present SIBIC imaging, only five ions per pixel are used to obtain the image. Such a low dose of ions can hardly decrease the charge pulse height. Therefore, image degradation in the previous IBIC during observation can be suppressed successfully by using our SIBIC technique.

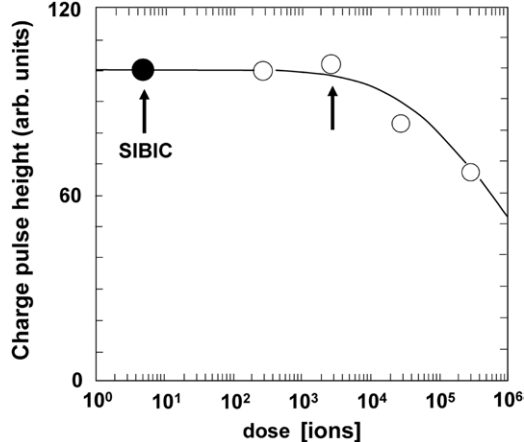


Figure 5. Average charge pulse height versus ion dose at the central area of the drain in the test device. Only five ions per pixel are used for SIBIC imaging, as indicated in the figure.

3.3. Application of SIMP to device diagnosis

The combination of the capability to sequentially collide a single ion on a particular device site and the SIBIC technique made it possible to apply SIMP to semiconductor device diagnosis.

3.3.1. Identification of soft-error sensitive junctions in static random access memory (SRAM) [13]. In order to identify soft-error (SE) sensitive sites, 3 MeV He single ions were irradiated on a 64 kbit SRAM (NASDA38510/91401XCR manufactured by NEC) with six transistor cells with a scanning step of $2 \mu\text{m}$. Since the SRAM was designed especially for space application, the SRAM was SE-immune against 3 MeV He irradiation at a supply voltage of 5 V. Therefore, the supply voltage to the radiation-hardened SRAM was reduced from 5 to 0.4 V to facilitate SE induction. As the supply voltage was reduced, the critical value of the voltage changed and the charge necessary to upset the cell became smaller. Thus, it was concluded that we can eventually scale down the SE immunity of SRAMs by reducing the supply voltage.

The circuit diagram and layout of the sample memory cell are shown in figures 6 and 7 [13]. p- and n-MOSFETs are located in the upper and lower half of the memory cell area, respectively. It should be noted that the drain junctions of the four MOSFETs in a flip-flop circuit are SE-sensitive; we denoted the drain junctions of the n-MOSFETs as An and Bn and those of the p-MOSFETs as Ap and Bp. Maps of error sites are shown in figure 8 [13]. The size of one pixel is $2.0 \times 2.0 \mu\text{m}^2$ and three single ions collide at each pixel. The number of detected SEs is indicated by the contrast of the pixel. The darkest contrast corresponds to three SEs resulting from three single-ion hits.

The correlation between error sites and the device layout is explained as follows. A reverse-biased junction can be SE-sensitive against ion incidence. If the memory cell is initially in the '1' logic state, nodes An and Bp, which are reverse biased can be SE-sensitive. Thus, error sites on the map in figure 8(a) reflect sites An and Bp. For the same reason, figure 8(b) reflects sites Ap and Bn. The SEs in the upper and lower half of

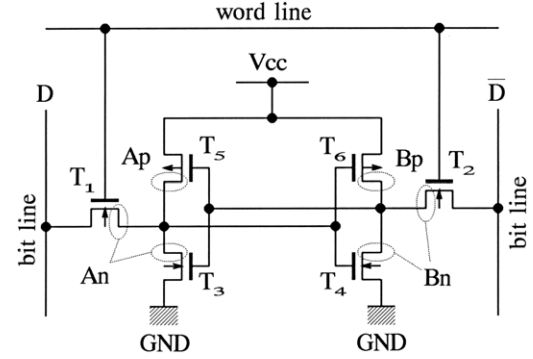


Figure 6. Circuit diagram of a memory cell in a 64 kbit SRAM target. Nodes An and Bn correspond to the error-sensitive junctions of n-MOSFETs, and nodes Ap and Bp correspond to those of p-MOSFETs. Broken lines in the circuit diagram indicate an Al layer, which has been eliminated in the layout (figure 7) for simplicity.

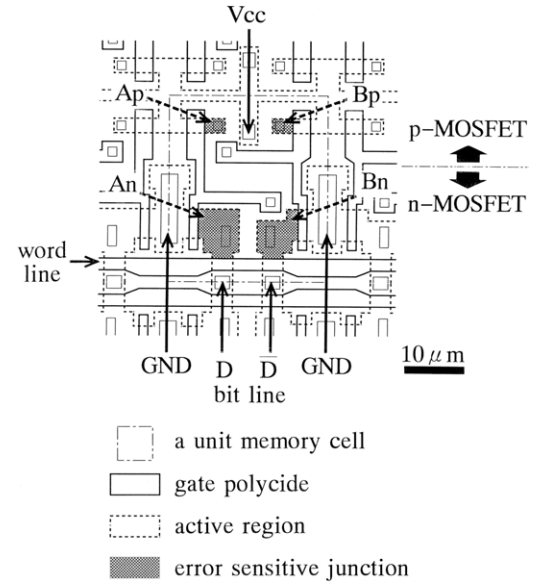


Figure 7. Layout of a memory cell in the 64 kbit SRAM target. p-MOSFETs are located in the upper half of the memory cell and n-MOSFETs, in the lower half. The error-sensitive junctions An, Ap, Bn and Bp are indicated by hatching.

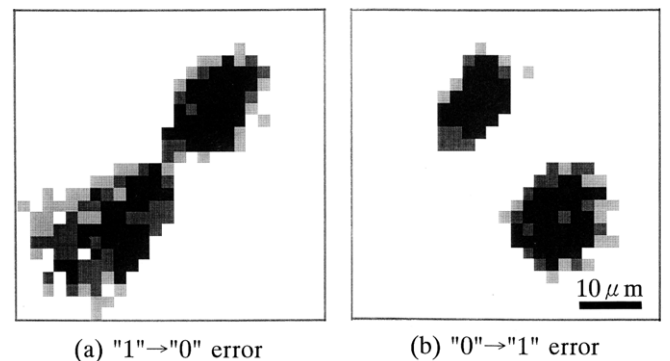


Figure 8. Error site maps corresponding to the initial logic states: (a) upsets from '1' to '0' and (b) upsets for '0' to '1'. Errors in the upper and lower regions are due to the upsets of p-and n-MOSFETs, respectively.

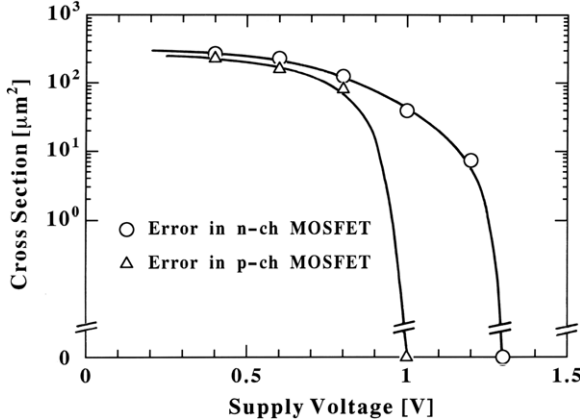


Figure 9. Soft-error cross section versus supply voltage to the SRAM. Circles and triangles represent the upsets of the n- and p-MOSFETs, respectively. The upsets of the n-MOSFETs have a higher threshold voltage than those of the p-MOSFETs.

the maps are due to the upsetting of the p- and n-MOSFETs, respectively.

We shall now discuss the difference in the SE immunity between the p- and n-MOSFETs. Here, we define the term ‘SE cross section’ as the area of the region where SE is induced. The SE cross section is estimated by counting the number of pixels in which errors were detected. Since the error sites can be clearly distinguished on the map for the n- and p-MOSFETs, we can easily estimate the respective SE cross sections by counting the number of error pixels in the lower and upper half of figure 8, respectively. Figure 9 shows the SE cross sections of each error mode as a function of the supply voltage. The cross sections are averages of ‘1’ to ‘0’ and ‘0’ to ‘1’ errors. As the supply voltage is increased, the cross sections of the p- and n-MOSFETs reach zero at 1.0 V and 1.3 V, respectively. Since a higher threshold voltage of SEs implies a higher sensitivity to SEs, we can conclude that an n-MOSFET is more error sensitive than a p-MOSFET. The reason for this is the larger drain junction areas of n-MOSFETs in comparison with those of the p-MOSFETs, as shown by the hatching in figure 7. In other words, the drain of the n-MOSFET has a larger solid angle for charges induced along an ion trajectory and this allows it to collect diffused charges more efficiently.

3.3.2. Site dependence of latch-up immunity in CMOS IC [12]. Among SEUs, latch-up is more serious in the sense that it often results in device burnout. As shown in figure 10, CMOS integrated circuits have inherently parasitic thyristors. The well–substrate junction is normally reverse biased and the parasitic thyristor is usually switched off. When a single ion strikes the well–substrate junction, a transient leakage current flows across the junction. If the current amplitude exceeds a critical value, the parasitic thyristor is triggered to the breakdown point and latch-up occurs. Thus, charges integrated due to the leakage current are a good measure to evaluate latch-up immunity at various sites of a CMOS IC. Throughout the experiments, single helium ions of 3 and 4.5 MeV were used. A CMOS IC (Motorola MC14049) with six inverter circuits was selected as the test device. The IC chip was exposed by removing the plastic package using a heated fuming acid.

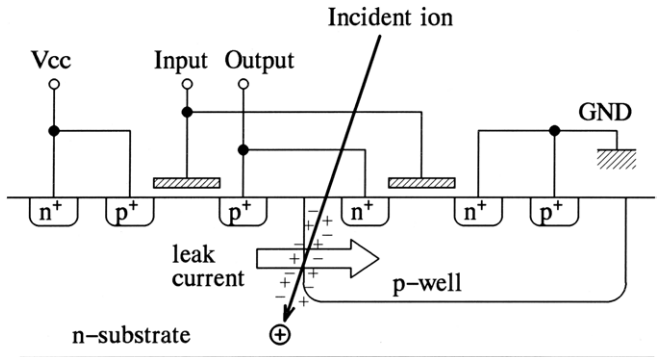


Figure 10. Schematic view of a CMOS inverter showing leakage induced by ion incidence.

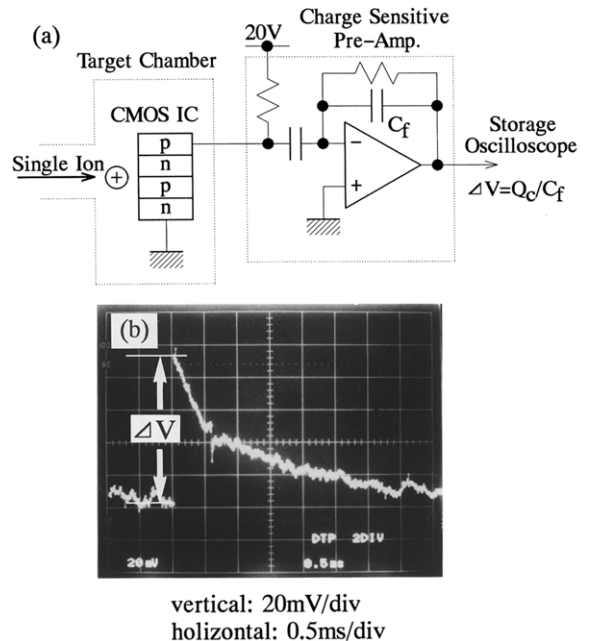


Figure 11. (a) Circuit for measuring collected charge. (b) Output waveform of a charge-sensitive preamplifier.

Figure 11(a) presents a schematic view of the circuit for measuring collected charges. A V_{cc} bias was applied to the test CMOS IC in the target chamber of the SIMP through a charge-sensitive preamplifier (Tennelec TC170). All the input terminals of the test IC were grounded. The leakage current induced by ion incidence was integrated and amplified by the preamplifier. The output waveforms were observed using a digital storage oscilloscope (IWATSU DS-6612). An output waveform of the preamplifier is shown in figure 11(b). The abrupt change in voltage waveform (ΔV) is due to charge collection upon ion incidence. The amount of charge can be obtained from the product of the voltage change ΔV and the feedback capacitance C_f in the preamplifier. We obtained a map of the induced charges by measuring the charge at each site in the test IC for every $100 \mu\text{m}$ interval.

Figure 12 shows the results of mapping. The amount of charges collected at each site is indicated quantitatively by the sizes of the circles. Figures 12(a) and (b) show the results for 3.0 MeV and 4.5 MeV helium ions, respectively. Both figures show that large amounts of charges are observed in the region

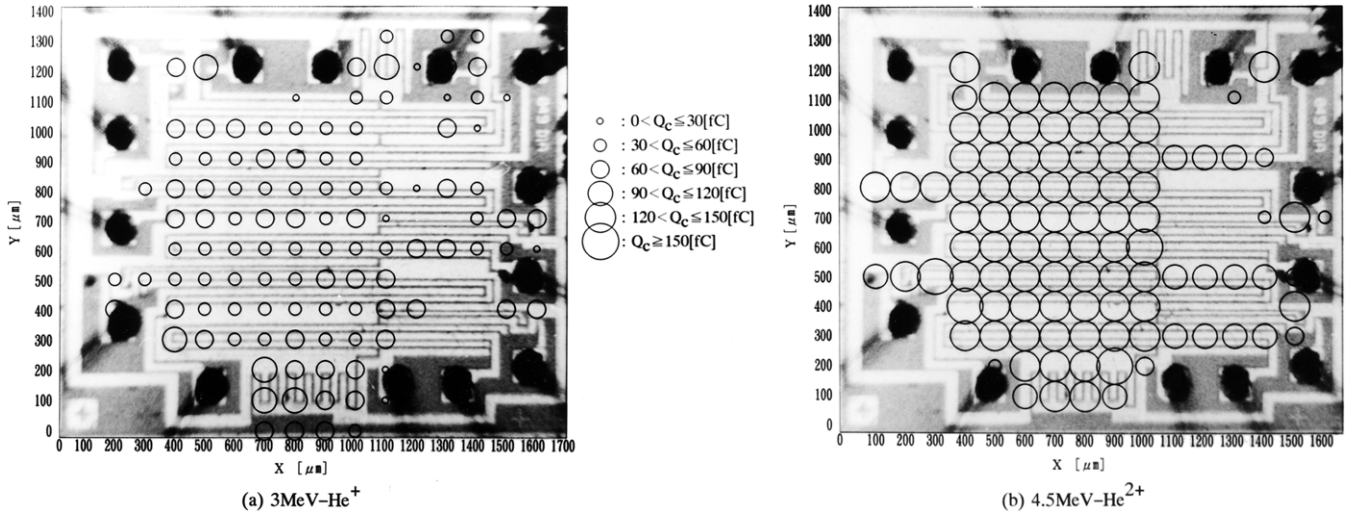


Figure 12. Charge collected upon incidence of single helium ions with an energy of (a) 3 and (b) 4.5 MeV.

corresponding to the p-type well. Since the amount of charge due to the leakage current can be regarded as a trigger for the latch-up, these maps can serve as a certain scale for studying latch-up susceptibility of the test IC.

3.3.3. Immunity of p-MOSFETs and n-MOSFETs against He SIIr [17]. Site-dependent radiation hardness of p-MOSFETs and n-MOSFETs on the same CMOS chip was investigated using the SIMP. A commercial inverter CMOS4007, shown in figure 13, was used as the test target in this study. Since this specimen was purchased in a commercial market, detailed information on the device structure, e.g. oxide thickness and doping concentration, are not known. The radiation tests were performed on each FET. Throughout this work, 2.0 MeV He single ions were used. The number of the irradiated ions was varied from 0 to $10^2 \mu\text{m}^{-2}$. The irradiated area was $240 \times 240 \mu\text{m}^{-2}$. During irradiation, all the pins were grounded. The irradiation sites were positioned by using SIBIC imaging.

Figure 14 shows the threshold voltage shift ΔV_{th} for both p-MOSFETs and n-MOSFETs as a function of the ion dose at room temperature. The threshold voltage was defined as the zero current intercept of the square root of the I_d versus V_g curves in the saturation mode. The threshold voltage V_{th} shifted in the negative direction for both p-MOSFETs and n-MOSFETs in proportion to the number of He ions. There are two major causes for the generation of radiation-induced interface charges, which are responsible for the V_{th} shift: the trapped holes in oxides and the charges trapped by interface states [45]. The slope represents the fragility of the target devices against ion irradiation. Since the slope for p-MOSFETs is steeper than that for n-MOSFETs, the former are more fragile than the latter in terms of the threshold voltage shift at room temperature.

The reason for the steeper slope, i.e. larger ΔV_{th} for p-MOSFETs, can be explained as follows. It is known that the net ΔV_{th} is the algebraic sum of voltage shifts due to the trapped holes, ΔV_{not} , and the trapped charges by the interface states, ΔV_{nit} [46]. It should also be noted that the

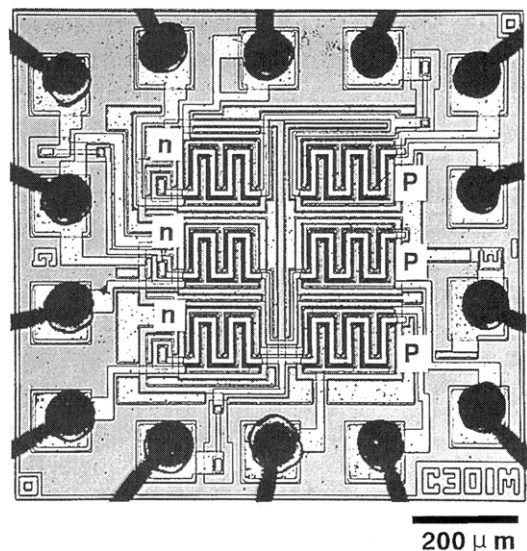


Figure 13. Optical micrograph of the test device.

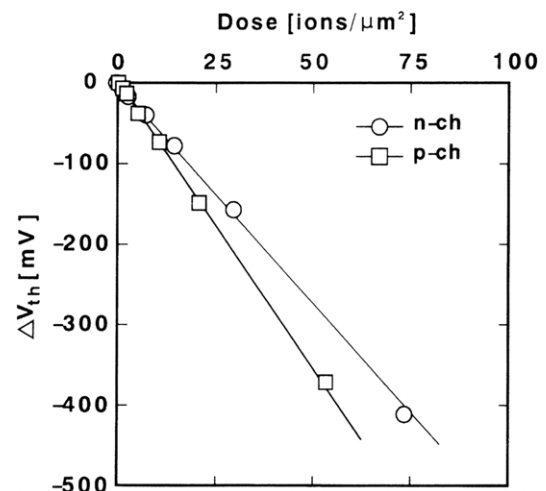


Figure 14. Threshold voltage shift ΔV_{th} for both p-MOSFETs and n-MOSFETs induced by ion irradiation.

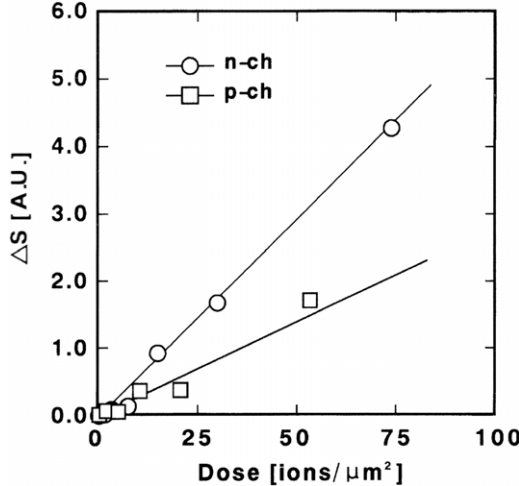


Figure 15. Subthreshold swing shift ΔS for both p-MOSFETs and n-MOSFETs induced by ion irradiation.

Pb centres responsible for the interface states are amphoteric in nature. They are donors in the lower part of the bandgap and acceptors in the upper part of the bandgap. Their occupancy depends on the value of the surface potential. The donor-like interface states are responsible for the V_{nit} shift of p-MOSFETs, while the acceptor-like interface states are responsible for the V_{nit} shift of n-MOSFETs. Therefore, ΔV_{nit} is negative for p-MOSFETs and positive for n-MOSFETs, while ΔV_{not} induced by trapped holes is always negative [47]. For p-MOSFETs, the sign of ΔV_{nit} is the same as that of ΔV_{not} , resulting in a larger ΔV_{th} . For n-MOSFETs, however, it is expected that the opposite signs of ΔV_{nit} and ΔV_{not} result in a relatively small shift in V_{th} . Thus, p-MOSFETs are more fragile than n-MOSFETs in terms of the threshold voltage shift.

Figure 15 shows the subthreshold swing shift, ΔS , for both p-MOSFETs and n-MOSFETs as a function of the ion dose. The subthreshold swing is defined as the change in the gate voltage necessary to reduce the transistor current by one decade. It is well known that the subthreshold swing, S , is proportional to the average interface state density, D_{it} , in the weak inversion region. The change in the interface state density induced by ion irradiation, ΔD_{it} , is given by

$$\Delta D_{\text{it}} = [C_{\text{ox}} \times / (kT \ln(10))] \Delta S, \quad (1)$$

where C_{ox} is the oxide capacitance and k the Boltzmann constant [48]. Although the exact interface state density cannot be estimated because of the lack of precise information on the device structure, the tendency of change in the mean interface state density can be understood by evaluating the change in the subthreshold swing before and after the ion irradiation. As shown in figure 15, the subthreshold swing S increases for both p-MOSFETs and n-MOSFETs as the number of He ions is increased, and ΔS for n-MOSFETs is higher than that for p-MOSFETs. This suggests that a larger number of interface states were induced by high-energy ions in n-MOSFETs rather than in p-MOSFETs.

The difference in ΔS between n-MOSFETs and p-MOSFETs can be attributed to the asymmetrical distribution

of the radiation-induced interface states in the midgap, which was found by Ma *et al* [49, 50]. According to their work, the density of the electron beam induced interface states in the upper half of the band gap is higher than that in the lower half of the band gap and the peak is located at 0.2–0.3 eV above the midgap. Since the interface states in the upper half of the bandgap are responsible for the degradation of S in n-MOSFETs and those in the lower half, for the degradation in p-MOSFETs, it is clear that n-MOSFETs are more susceptible than p-MOSFETs to the degradation of the subthreshold swing S .

All these conclusions concerning the radiation immunity of MOSFETs were obtained from the sequential counting of the incident single ions.

3.3.4. Quantitative analysis of degradation in Schottky diode characteristics induced by He SIIr [21]. Metal–semiconductor contacts (M–S contacts) are key structures functioning as ohmic contacts in semiconductor devices and Schottky diodes (SDs). To investigate radiation effects on M–S contact characteristics is important for two reasons. One is the necessity to better understand the radiation immunity of SDs themselves, because they are used for various devices such as mixers, sensors and electronic switches. The second reason is that SDs are well defined in the sense that their device characteristics are well understood and radiation effects can be analysed quantitatively, as will be shown later.

The experimental procedure consists of three steps: (1) Schottky diode fabrication, (2) MeV He SIIr and *in situ* measurement of current (I)–voltage (V) characteristics of SDs and (3) curve fitting of the measured I – V data to extract the radiation effect quantitatively. PtSi/n-Si(100) SDs with a circular contact of 50 μm diameter were prepared under good experimental conditions. In order to find a quantitative relationship between the number of implanted single ions and radiation effects, it is important to implant a well-defined number of ions into a well-defined Schottky junction. For precise control of the number, we used the SIMP. For high-precision aiming of the defined area to be bombarded with the ions, SIBIC imaging was used. He single ions of 2 MeV were irradiated onto the SDs at ion doses ranging from 10^2 to 10^5 ions. During ion irradiation and I – V measurement, the sample temperature was maintained at room temperature. Typical I – V characteristics are shown in figure 16.

After ion irradiation, we quantitatively analysed the I – V characteristics by least square curve fitting. In the curve fitting, we assumed that the forward current consists of two components: thermionic emission current and recombination current [51]. In fitting a theoretical I – V curve to an experimental one, the program finds by iteration a set of three parameters: real barrier height (ϕ_{ho}), recombination current density ($J_{\text{r}0}$) and series resistance (R_s).

In order to estimate the number of recombination centres in the SD induced by SIIr on the basis of the experimental results and the curve fitting, we derived the following relation between the recombination centre density (N_r) and the recombination current density ($J_{\text{r}0}$):

$$N_r = 2J_{\text{r}0}/v_{\text{th}}\sigma q n_i w, \quad (2)$$

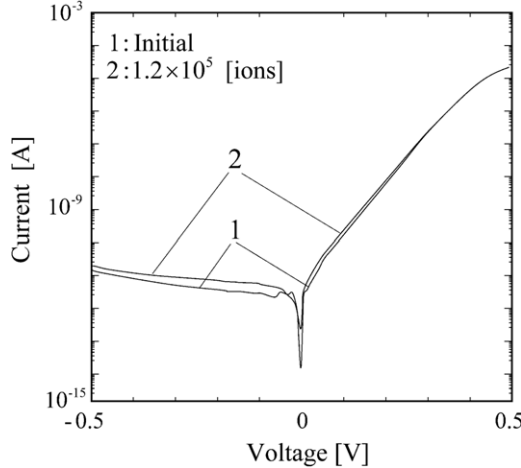


Figure 16. I - V characteristics of a PtSi/n-Si Schottky diode before and after ion irradiation. He single ions were irradiated at an acceleration energy of 2 MeV to a dose of 1.2×10^5 ions.

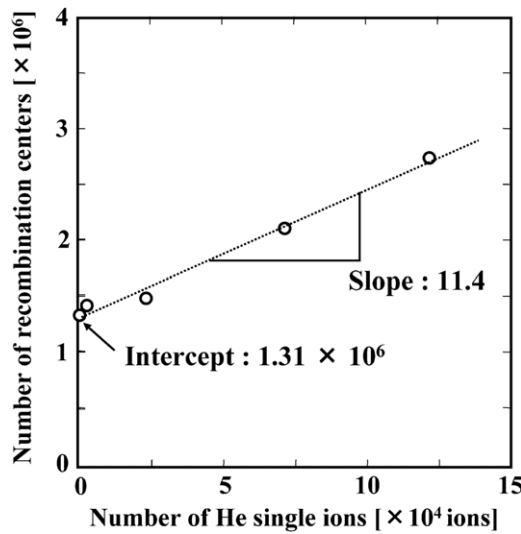


Figure 17. Relationship between the number of He single ions and the number of recombination centres.

where v_{th} is the thermal velocity of carriers, σ the carrier capture cross section of recombination centres, q the electronic charge, n_i intrinsic carrier density and w the depletion layer width. This equation is based on the following assumptions. First, there is only one defect energy level and capture cross section. Second, the recombination centre is at the midgap of Si. In the calculation of N_r from J_{t0} , we assumed v_{th} to be 10^7 cm s^{-1} and σ to be 10^{-15} cm^{-2} .

Figure 17 shows the relationship between the number of implanted He single ions and the number of recombination centres (N_r) in the depletion region of the SD (note that N_r is the product of N_r and the SD contact area). The dotted line in this figure is the least square fit to the experimental plots. It is obvious that there is a very good linearity between N_r and the number of He single ions. The slope of the dotted line, 11.4, implies an average number of recombination centres induced by a He single ion at an energy of 2 MeV at room temperature. This value would depend on the ion species, acceleration energies and irradiation temperature.

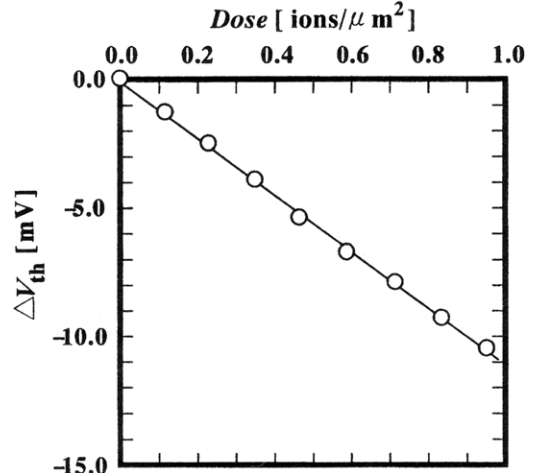


Figure 18. Threshold voltage shift ΔV_{th} induced by SIIr in a test n-MOSFET.

Particularly, the irradiation temperature must have played an important role in the relaxation process during and after the ion collision cascade. An important aspect of figure 17 is that if we plot a quantity related to a process or device function, the slope of the dotted line in figure 3 can be regarded as an index of device immunity against ion irradiation, e.g. the slope would be high for a ‘fragile’ device, as pointed out previously.

The intercept, 1.31×10^6 , found by extrapolating the experimental plots in figure 17 to zero ions yields the number of recombination centres that exist at the initial M/S interface. The initial number obtained directly from the I - V characteristic of the SD before ion irradiation was 1.27×10^6 . The coincidence between the two values is quite good. This suggests that even if the initial value is below the detection limit, the extrapolation to zero ions gives an alternative method to evaluate the initial value. Thus, the slope and the intercept at the vertical axis in the linear relationship, as shown in figure 17, can be powerful tools for process and device diagnosis.

3.3.5. Quantitative analysis of radiation-induced Si/SiO_2 interface defects by MeV He SIIr [20, 24, 25].

Based on the experimental setup, discussed in section 3.3.3 in this section, it is possible to carry out a more quantitative investigation of ion irradiation effects in MOSFETs in terms of interface defects such as oxide trapped holes and interface states.

We first show the influence of ion irradiation with an extremely low number of ions on the characteristics of MOSFETs. We then separately estimate the number of oxide trapped holes and the interface states induced by the MeV He SIIr. The experimental condition is identical to that in section 3.3.3, except for the ion dose. The number of irradiated ions was varied from 0 to $1.0 \text{ ions } \mu\text{m}^{-2}$. Figure 18 shows the threshold voltage shift ΔV_{th} for an n-MOSFET as a function of the ion dose. Although the ion dose is extremely low, the threshold voltage shift in the negative direction is perfectly proportional to the number of He ions. The two charge components can be separated by analysing the subthreshold I - V characteristics [46]. Figure 19 shows the net threshold voltage shift and the contributions from the trapped-oxide

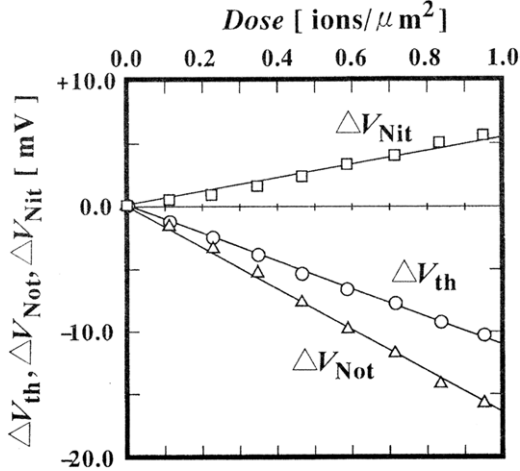


Figure 19. Contributions of voltage shift due to the trapped-oxide charge ΔV_{not} and the interface traps ΔV_{nit} to the net threshold voltage shift ΔV_{th} .

charge, ΔV_{not} , and the interface traps, ΔV_{nit} . ΔV_{not} shifts in the negative direction because of hole trapping, while ΔV_{nit} shifts in the positive direction because of electron trapping by the interface states. Since ΔV_{not} is larger than ΔV_{nit} , V_{th} shifts in the negative direction on the whole. Again, it is clear that both ΔV_{not} and ΔV_{nit} change in perfect proportion to the number of He ions.

Once the relationship between ΔV_{not} and the ion dose is known, the number of oxide trapped charges induced by a single He ion, N_{not} , can be determined by the following equation:

$$N_{\text{not}} = \frac{\Delta V_{\text{not}}}{D} \cdot \frac{C_{\text{ox}}}{q}. \quad (3)$$

Here, D (ions cm^{-2}) is the ion dose and C_{ox} (F cm^{-2}) is the capacitance of the oxide per unit area. Similarly, the number of interface states induced by a single He ion, N_{sit} , can be estimated by

$$N_{\text{sit}} = \frac{\Delta V_{\text{nit}}}{D} \frac{C_{\text{ox}}}{q}. \quad (4)$$

It should be noted that N_{sit} represents the increase in the total number of interface states between midgap and the Fermi level. From the above equations, the number of oxide trapped charges induced by a single He ion was estimated to be about 28 while the number of interface states was estimated to be about 9. We have not yet carried out work to correlate these numbers with atomistic models of SiO_2/Si interface defects.

4. Single-ion implantation (SII)

4.1. Introduction

In general, a function value, x , of a device, e.g. threshold voltage and capacitance, fluctuates around a designed value due to device process fluctuations. If the device fluctuation is a result of the summation of various independent factors, the distribution, i.e. the number of devices, n , with a function value x , is approximately expressed by a Gaussian function as

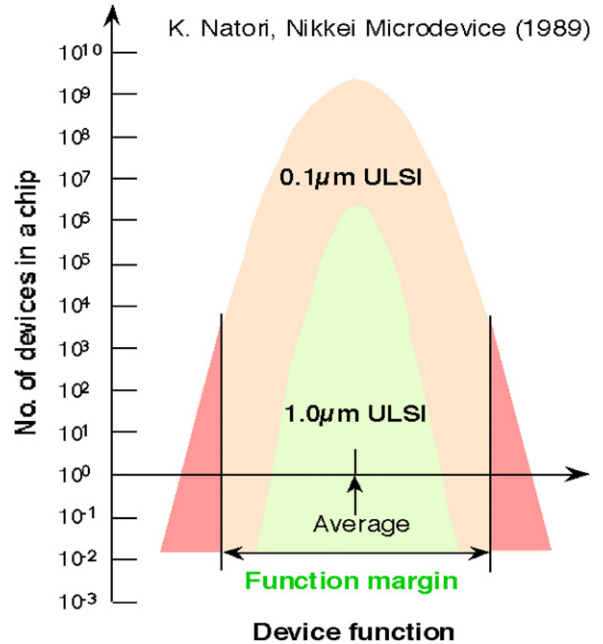


Figure 20. Motivation to develop SII—the device function value fluctuates around the designed value due to device process fluctuations, which result in the degradation of the device yield.

follows [52, 53]:

$$n \propto e^{-(x-x_m)^2/2\sigma^2}, \quad (5)$$

where x_m is the mean value of the function and σ the standard deviation. This distribution is expressed as a concave-down parabolic curve in semi-logarithmic coordinates, as shown in figure 20. If the device function distributes outside the window of a proper circuit function, the device is said to be dead. The area under the parabolic curve and outside the window gives the average number of failure devices. σ depends on the maturity of the processes and increases with a decrease in the minimum feature size of the device. As the integration level is increased, the curve shifts upwards and σ increases. Therefore, the yield defined as the probability of no failure devices on a chip in a Poisson distribution decreases exponentially, eventually limiting further miniaturization of devices.

Our motivation for developing the SII was to solve the problem associated with the increase in the fluctuation of the dopant number in an ultra-fine semiconductor area. Here, by ‘ultra-fine’ we mean a size less than $0.1 \mu\text{m}$ [27].

As the device size is reduced to less than $0.1 \mu\text{m}$, fluctuation in doping concentration seriously affects device characteristics. Since conventional ion implantation uses a high current and uniform ion beam, the fluctuation in the number of dopants is inevitable due to the Poisson distribution. Suppose N is the average dopant number in a device active region. Then, the fluctuation in the dopant number, $\Delta N/N$, is given as follows:

$$\frac{\Delta N}{N} = \frac{\sqrt{N}}{N} = \frac{1}{\sqrt{N}}. \quad (6)$$

In CMOS devices that will be fabricated in the near future, the device active region would be of quantum size and they would

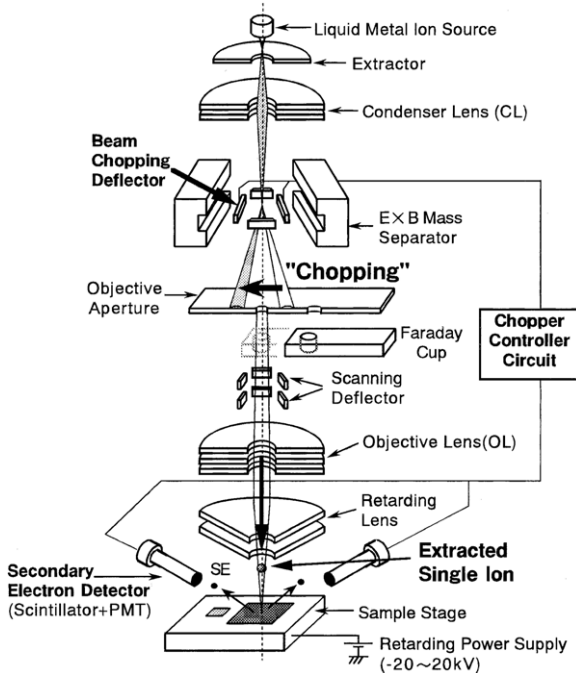


Figure 21. Optics and principle of SII using an FIB system.

contain only a limited number of dopant atoms. If we assume a doping concentration of 1×10^{18} atoms cm^{-3} in an active region of a quantum size device ($100 \times 50 \times 50 \text{ nm}^3$), the total number of dopant ions would be 250 and the fluctuation due to the Poisson distribution would amount to 6.3%. This could impact the yield in device manufacture.

To reduce the fluctuation, it is necessary to implant dopant ions one by one until the necessary number is reached. In order to realize the function of implanting dopant ions one by one with an areal resolution greater than $0.1 \mu\text{m}$, the SIMP discussed in section 3 would not be suitable. We therefore decided to resort to a FIB system.

4.2. Key technologies to remodel FIB system into SII [28, 29]

4.2.1. Principle of SII. In figure 21, we show the optics of the FIB system used for the SII. The FIB column consists of a LMIS; a condenser lens; an $E \times B$ mass separator that contains a beam chopping deflector, for single-ion extraction, and an objective aperture; an objective lens; and deflectors for scanning the ion beam. It is possible to produce ion beams of Be, B, Si, P, As, Ga, Au and other ion species by selecting appropriate materials for the LMIS [54–56]. Our original LMISs were also used for yielding other ion species such as Fe, Co, Ni, In, Sb and Pt. The accelerating voltage of the ion beam was 30 kV for a single charge and 60 kV for double charges. The principle of beam chopping to extract single ions is the same as that for the SIMP.

The number of ions that passed through the aperture by chopping was proportional to the ion-beam current and the aperture opening and inversely proportional to the transient time of chopping. Thus, the number of ions extracted by a single chop can be set to 1 or 0 under optimized parameter

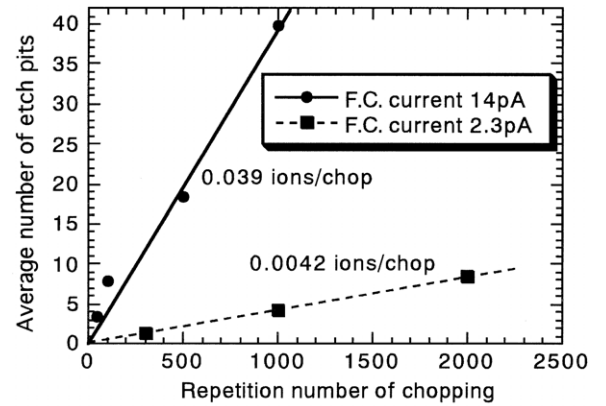


Figure 22. Relationship between the number of etch pits in a fission track detector, CR-39, induced by single-ion incidence and the chopping repetition number.

conditions. The trajectory of the extracted single ions is focused by the objective lens in the same manner as that used in conventional FIB and the single ions are implanted into fine semiconductor regions. Whether or not a single ion is successfully implanted into the sample is confirmed by detecting secondary electrons (SEs) that are ejected from the sample upon ion incidence.

In order to control the number of implanted ions accurately in the SII, we must satisfy the following two conditions: (1) the number of ions extracted by a single chop must be one or zero and (2) the incidence of the extracted ions must be detected completely. The fulfilment of these two conditions is discussed in later sections.

4.2.2. Singularity of extracted single ions. In order to meet the above-mentioned requirements, we need to discuss a means to detect ion incidence easily but accurately and establish a guiding principle to extract only one ion per operation; by this we do not mean a single chop but multiple chops, as discussed below.

As a target to confirm single-ion incidence, we selected CR-39 [31], which has been used so far as a fission track detector. Energetic ions penetrate CR-39 and generate potential damage at the site of incidence. The damaged regions along the ion tracks appear as etch pits with enlarged diameters after chemical etching in heated NaOH solution. Circular etch pits approximately 200 nm in diameter are observed by AFM. This method was also used for measuring the accuracy of aiming at a target. The relationship between the average number of etch pits and the repetition number of chopping is shown in figure 22. The number of etch pits increased linearly with the repetition number of chopping at ion-beam currents of 2 and 14 pA. The average number of ions extracted by a single chop (N_{ext}) was estimated from the gradient of the lines in figure 22 as 0.0042 ions/chop for the 2 pA beam current and 0.039 ions/chop for the 14 pA one.

The guiding principle to extract only one ion per operation was formulated as follows. We defined the singularity S as the conditional probability that the number of ions extracted by a single chop equals 1 under the condition that a certain

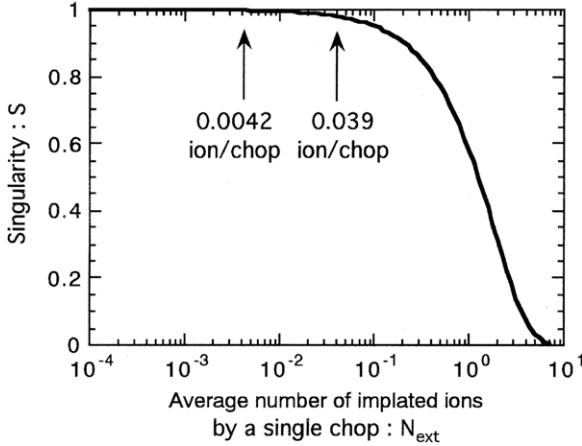


Figure 23. Singularity of extracted ions as a function of the average number of implanted ions by a single chop. Singularity of approximately 100% is expected under the average number of ions by a single chop estimated from figure 22.

number of ions have already been extracted. We also defined the probability that k ions are extracted by a single chop as $P_{\text{ext}}(k)$; then, the singularity S is expressed as

$$S = \frac{P_{\text{ext}}(k=1)}{P_{\text{ext}}(k \geq 1)} = \frac{P_{\text{ext}}(1)}{1 - P_{\text{ext}}(0)}. \quad (7)$$

Since the extraction of single ions from each chop occurs randomly, we assumed that the probability $P_{\text{ext}}(k)$ obeys a Poisson distribution, namely,

$$P_{\text{ext}}(k) = \frac{N_{\text{ext}}^k \exp(-N_{\text{ext}})}{k!}, \quad (8)$$

where N_{ext} is the average number of ions extracted by a single chop. Thus, S is expressed by N_{ext} as follows:

$$S = \frac{N_{\text{ext}} \exp(-N_{\text{ext}})}{1 - \exp(-N_{\text{ext}})}. \quad (9)$$

The singularity calculated by equation (9) as a function of the average number of ions extracted by a single chop is shown in figure 23.

Since it is estimated from figure 22 that the average number of ions extracted by a single chop is 0.039 ions/chop and 0.0042 ions/chop under ion-beam currents of 14 pA and 2 pA, respectively, the singularity S under these conditions is regarded as 1, as shown in figure 23. Therefore, we consider that the first condition necessary for the SII, namely, the number of ions extracted by a single chop must be 1 or 0, is satisfied under these conditions. On the other hand, the singularity S is estimated as 0.946 for N_{ext} of 0.11 ions/chop. In other words, the probability that multiple ions are extracted by a single chop is approximately 5%. Thus, the controllability of the implanted ion number deteriorates for a larger value of N_{ext} .

4.2.3. Controllability of implanted ion number. In this section, we focus on the second condition, namely, the detection efficiency of single-ion incidence. This efficiency

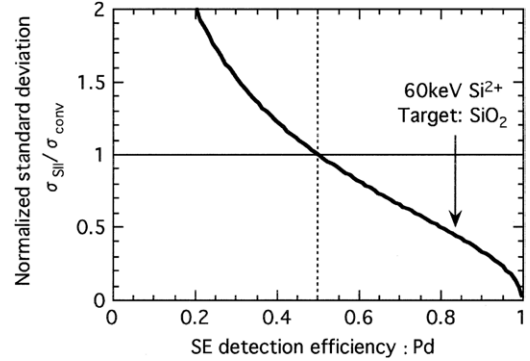


Figure 24. Standard deviation of number of ions implanted by SII as a function of the detection efficiency of secondary electrons. The standard deviation is normalized by a Poisson distribution.

must be 1 to ensure perfect control of the single-ion number, but is influenced by two factors: the noise in the PMT used for detecting SEs and the detection efficiency of SEs emitted from the sample upon ion incidence.

It is well known that PMTs produce noise pulses that are generally referred to as ‘dark counts’. These dark counts lead to incorrect recognition of single-ion incidence. In order to reduce the effect of dark counts, we measured the time of flight of ions by synchronizing the chopping with ion incidence. We found that the time window of 0.7 μs, which starts 500 ns after the instant of chopping, is appropriate for eliminating the dark counts for a 60 keV Si²⁺ ion beam in the present SII system.

The second factor that influences the detection efficiency of single-ion incidence is the detection efficiency of SEs that is less than one. Here, we define the detection efficiency of SEs, P_d , as the average count of SE detection by the incidence of a single ion. There are at least four reasons for the loss in P_d . They are the geometrical factors of the SE detection system, the contingent nature of SE emission from sample materials, incident ion species and energy. For example, it is reported that a 60 keV Ne⁺ ion ejects approximately 2.5 SEs on an average from a clean metal (Mo) target [57]. Even under the perfect condition of 100% SE detection and no dark counts, P_d remains less than 1. Figure 24 shows the correlation between the SE detection efficiency, P_d , and the fluctuation in the implanted ion number by the SII (standard deviation normalized by that of the conventional I/I). It is clear that if P_d remains 0.5, the fluctuation in the implanted ion number by the SII will become the same as that by conventional I/I and, consequently, the advantages of using SII would be completely lost. In our group, we are currently investigating a different ion incidence detection system that has 100% efficiency [58].

4.2.4. Aiming precision [34]. An outline of the FIB optics is schematically shown in figure 25 for the original and the modified single-ion implanter. The ion optics comprise a crossover point at which the ion beam emitted from a LMIS is focused by condenser lens (CL), chopping electrode, objective lens (OL) electrode, OL aperture and sample stage. The ratio of the transverse dimensions of the final image formed by OL to the corresponding dimensions of the image at the crossover point is defined as the lateral magnification, M ($\cong l_2/l_1$), as

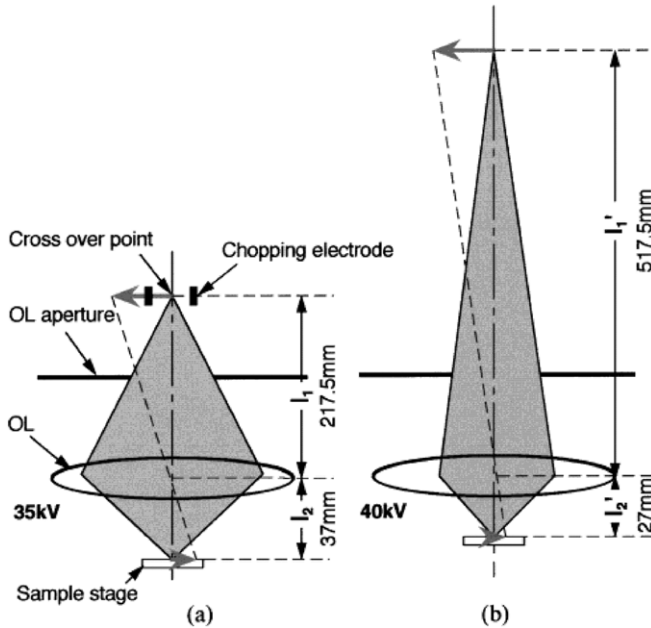


Figure 25. Modification in FIB optics for higher aiming precision in the SII. (a) Before modification, (b) after modification.

indicated in figure 25. Here, l_1 is the length between the crossover point and the centre of the OL electrode and l_2 , the length between the centre of the OL electrode and the target. In the original FIB optics, M was designed such that l_2/l_1 was $37\text{ mm}/217.5\text{ mm} = 1/3$. This configuration yielded an aiming precision of 170 nm. For improved performance in the modified optics, we carefully selected l_1 and l_2 to be 517.5 mm and 27 mm, respectively. Consequently, the magnification of OL improved to $l_1/l_2 = 27\text{ mm}/517.5\text{ mm} = 1/19$, which corresponded to one-third the previous magnification. By this improvement, the beam diameter evaluated by the scanning ion microscope (SIM) reached less than 20 nm. Figures 26(a) and (c) show the AFM images of the etch pits in the CR-39 that were acquired for the FIB optics before and after modification. The 60 keV Si ions were irradiated at 1 μm intervals and the chopping was repeated at the rate of 200 chops/site. Figure 26(b) and (d) show the histograms of the deviation of the incident sites from the target sites. Around 96% of the single ions were implanted on a region within 100 nm in the modified optics. The average deviation in the single-ion-incident site was suppressed to only 60 nm, which corresponded to one-third the value before modification. In accordance with the modification in the ion optics, the time windows to reduce the effect of the dark counts of the PMT were set between 1000 and 1500 ns.

4.3. Applications

The most straightforward application of the SII is to suppress the fluctuations associated with dopants. We first applied the SII to suppress the fluctuation in the dopant number over a fine semiconductor area and then used it to yield a novel semiconductor with an ordered dopant array. For these two applications, we used test FETs, which will be described later, and confirmed that the devices exhibited accumulation-mode

n-channel transistor behaviour. We also confirmed that the Fermi level in the channels is controlled by the back-gate and drain bias [35].

4.3.1. Trimming conductance in sub-micron-size resistors to reduce fluctuation [36]. In this study, we attempted trimming the conductance fluctuation in a very fine resistor by using the SII. By ‘resistor’ we mean an active region in a semiconductor device, e.g. a channel region in a MOSFET. First, we precisely evaluated the conductance increment per single dopant ion. Then we measured the conductance of very fine semiconductor resistors and obtained a statistical distribution. Finally, we implanted in each test resistor the number of single ions necessary to tailor the conductance to a certain value on the higher side of the initial conductance distribution. Figure 27 shows the structure of the test resistors. In order to fabricate fine semiconductor resistors accurately, we used a very thin ($0.09\text{ }\mu\text{m}$) n-type Si crystal specially prepared by the SIMOX (Separation by IMplantation of OXygen) method, and this thin Si crystal was patterned to form the test resistors.

In the first step, to measure the conductance increment per dopant ion ($\partial g/\partial N_D$), test resistors with a relatively large scale ($1\text{ }\mu\text{m}$ wide and $2\text{ }\mu\text{m}$ long) were used to minimize the disturbance due to device size fluctuation. Around 10–250 phosphorus ions were implanted at 30 kV on areas of $0.5 \times 0.5\text{ }\mu\text{m}^2$ in $1\text{ }\mu\text{m} \times 2\text{ }\mu\text{m}$ resistors. The implanted samples were subsequently annealed at $900\text{ }^\circ\text{C}$ for 5 min in N_2 ambient to electrically activate the implanted P atoms. Under this annealing condition, the average electrical activation ratio (η) was 90%.

In the second step, to investigate the influence of size reduction on the statistical fluctuation of conductance, smaller resistors ($0.3\text{ }\mu\text{m} \times 1.2\text{ }\mu\text{m}$) were fabricated. Prior to SII for tailoring conductance, the initial conductance of 22 fine resistors was measured to obtain a statistical distribution. The number of ions necessary to trim the conductance was calculated for each resistor based on the experimentally obtained $\partial g/\partial N_D$. The necessary number of ions were implanted one by one into each resistor per $0.3 \times 0.3\text{ }\mu\text{m}^2$ site. After heat treatment of the implanted specimens for electrical activation, the conductance was measured in the same manner. The conductance distribution after the modification by the SII was compared with the initial one from the viewpoint of fluctuation.

Figure 28 shows the relationship between the number of implanted ions and the conductance in the larger test resistors. The conductance (g) was found to increase linearly with the dopant atom number. The increment of g per impurity ion ($\partial g/\partial N_D$) was found to be $18\text{ nS ion}^{-1} (0.5\text{ }\mu\text{m})^{-2}$, which coincided reasonably well with the calculated value $\partial g/\partial N_D = q\mu\eta(W/L) = 22\text{ nS ion}^{-1} (0.5\text{ }\mu\text{m})^{-2}$ using the nominal device size, the experimentally determined mobility (μ) and the electrical activation ratio (η) values.

Figure 29 shows the histograms of the deviation of the conductance from the mean value for the 22 smaller resistors before and after conductance trimming. As shown in figure 29(a), the initial conductance deviated considerably from the mean value. The average conductance (g^i), the

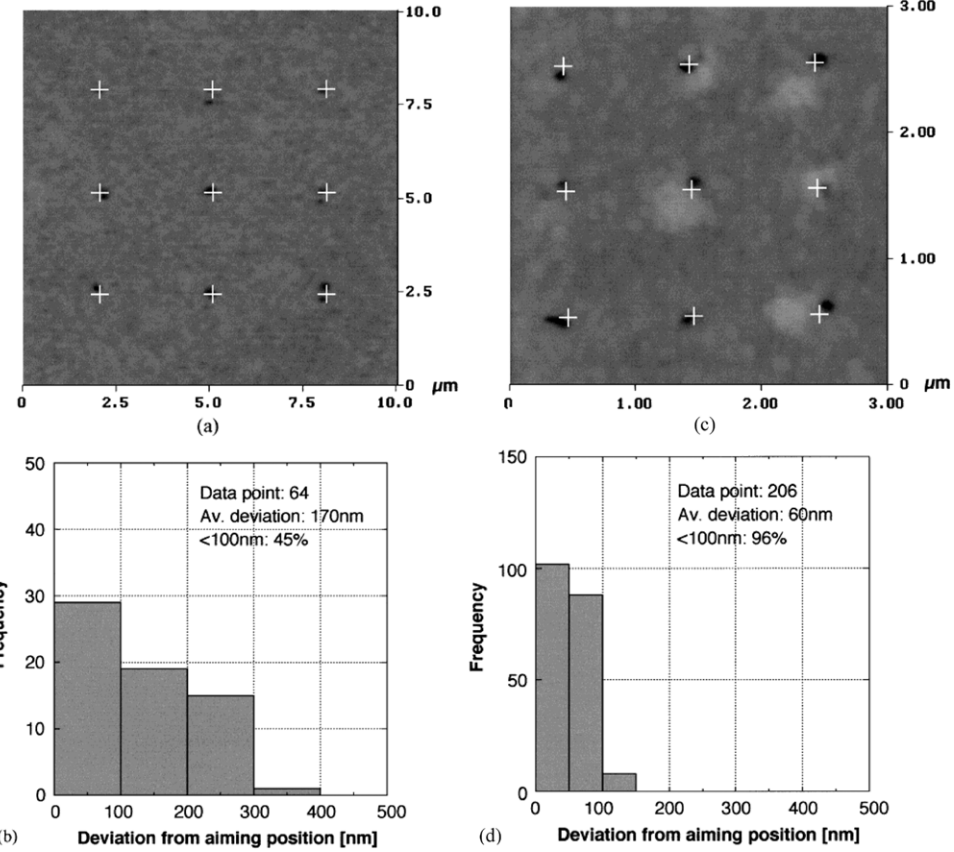


Figure 26. Evaluation of aiming precision in the SII before and after the remodelling of ion optics. AFM image of etch pits in CR39 induced by single-ion incidence: (a) before, (c) after. Histogram of deviation of ion-incident sites from the target sites: (b) before, (d) after.

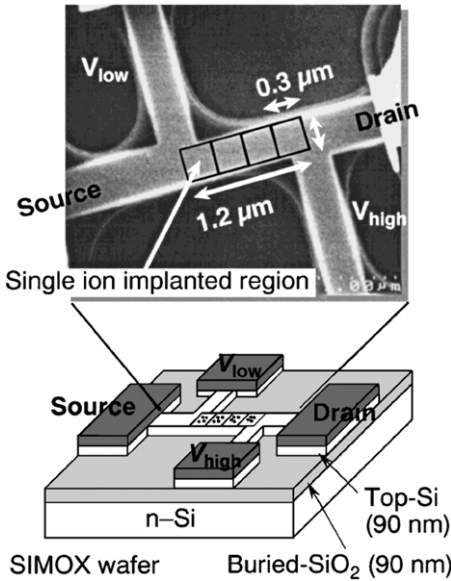


Figure 27. Structure of test resistor for investigating the influence of fluctuation in electrical conductance.

standard deviation of g^i (σ^i) and the fluctuation ($f^i = \sigma^i/g^i$) were found to be 381 nS, 239 nS and 0.63, respectively. Based on the experimental increment of the conductance per ion, the number of ions necessary to trim the conductance was calculated for each test resistor. Then, $2-13 \text{ ions}/(0.3 \mu\text{m})^2$

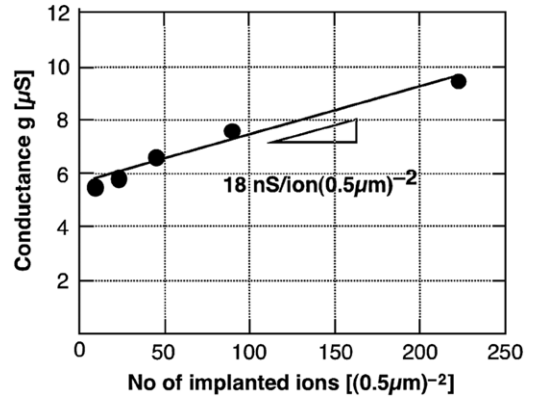


Figure 28. Correlation between the conductance of a test resistor and the number of implanted single dopant ions to be used for conductance tailoring.

were implanted into the initial test resistors so that we could obtain an average conductance of 700 nS. As shown in figure 29(b), the conductance distribution was much narrower than the initial one. The three quantities defined after the trimming— g^f , σ^f and f^f —were evaluated to be 665 nS, 88 nS and 0.13, respectively. It was found that the initial conductance fluctuation of 63% was reduced to only 13%. These experimental results lead us to the conclusion that the inherent fluctuation of electrical properties in a fine semiconductor region can be trimmed by implanting the necessary number of dopant atoms by SII.

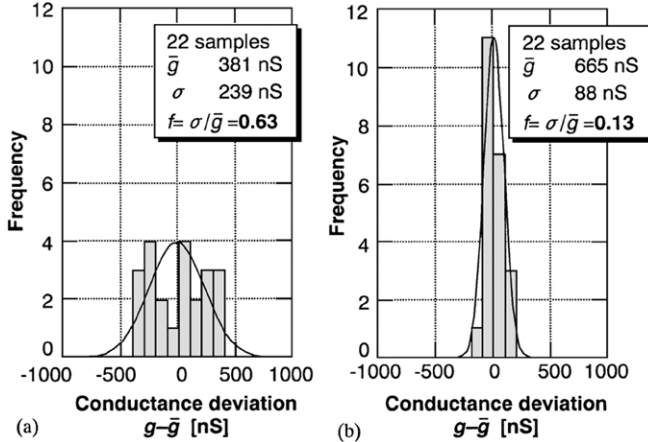


Figure 29. Statistical distribution of conductance measured for the 22 test resistors. (a) Initial conductance distribution. Fluctuation of the conductance around the mean value is mainly due to the fluctuation in the number and position of dopant atoms. (b) Conductance distribution after tailoring of conductance by sequential dopant ion implantation. Control of both the number and position of the dopant atoms is remarkable in reducing fluctuation.

We shall now discuss the origin of conductance fluctuation before (f_{cal}^i) and after tailoring (f_{cal}^f). f_{cal}^i is composed of impurity number fluctuation (f_{num}), impurity position fluctuation (f_{pos}), device size fluctuation (f_{size}) and measurement fluctuation (f_{meas}), and it is expressed as follows:

$$f_{\text{cal}}^i = \sqrt{f_{\text{num}}^2 + f_{\text{pos}}^2 + f_{\text{size}}^2 + f_{\text{meas}}^2}. \quad (10)$$

Here, f_{num} is expressed as $1/\sqrt{N_D}$, assuming that the dopant atoms in a fine semiconductor region obey a Poisson distribution. The initial average number (N_D) of impurities in the channel region ($0.3 \times 1.2 \mu\text{m}^2$) is estimated to be 16 from the nominal resistivity value. Then, f_{num} is obtained as $1/\sqrt{16} = 0.25$. With regard to f_{pos} , according to a computer simulation of device function [59], it is reported that the effect of the impurity position fluctuation becomes dominant as the channel impurity number is decreased. Based on this result, f_{pos} was estimated to be 0.5 for our experimental conditions. f_{size} was estimated to be 0.13 by directly observing the feature of each resistor using a SEM. f_{meas} was estimated to be 0.02 based on the scattering of the measured conductance value. By summing up all the components, we obtained a value of 0.57 for f_{cal}^i . Although there remains a small discrepancy between the experimental and the calculated values, there is no doubt that f_{num} and f_{pos} are the primary origins of the fluctuation, since their contribution is much larger than that of the other components.

The origin of the fluctuation (f_{cal}^f) in the conductance tailored by the SII is analysed in the same manner. f_{cal}^f is expressed as follows:

$$f_{\text{cal}}^f = \sqrt{f_{\text{SII}}^2 + f_{\text{pos}}^2 + f_{\text{ann}}^2 + f_{\text{meas}}^2}. \quad (11)$$

Here, f_{SII} is the fluctuation in the implanted ion number due to the less-than-one SE detection efficiency (ξ) in the SII and f_{ann} , the fluctuation induced in annealing for the electrical

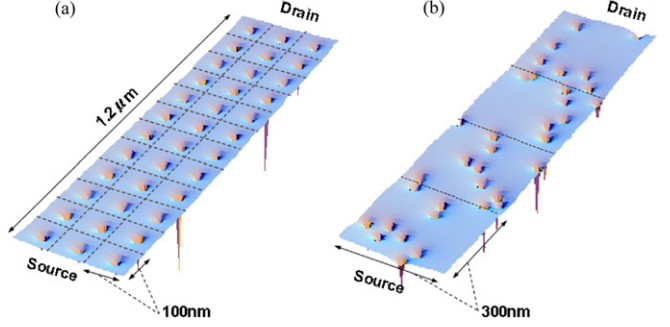


Figure 30. Calculated potential distribution of the channel region. (a) Potential distribution of the ordered dopant array. Energy is measured upwards. Phosphorus single ions were implanted at a pitch of 100 nm by SII. (b) Potential distribution of the conventional random distribution of phosphorus atoms.

activation of dopants. f_{SII} can be assessed based on our previous analysis of the relationship between the SE detection efficiency and f_{SII} . By investigating the proper value for each component, we found that f_{cal}^f could be evaluated to be 0.29. This is, however, much larger than the experimental one, $f_{\text{exp}}^f = 0.13$.

The reason for this large discrepancy is believed to be the overestimation of f_{pos} in SII specimens in which single ions were implanted at intervals of $0.3 \mu\text{m}$, where the impurity positions were not random. This clearly shows the importance of controlling not only the impurity atom number but also their positions.

4.3.2. Enhancing semiconductor device performance using ordered dopant arrays [37]. By reducing the fluctuation in a fine semiconductor device by means of SII, as discussed above, we found that the control of not only the dopant atom number but also its position is important. In this section, we demonstrate the creation of a novel semiconductor with ordered dopant arrays and the effect of these arrays on enhancing semiconductor device performance.

For this study, we used test FETs similar to those used previously. Before SII, the initial threshold voltage (V_{th}^i) was evaluated by the extrapolation of the linear part of the curve to the V_g axis in the V_g dependence of I_d under a certain V_d of 0.1 V.

By SII, doubly charged P single ions were implanted one by one at 30 kV into the channel region at a centre-to-centre distance (pitch) of 100 nm through the 25 nm thick surface oxide, as shown in figure 30(a), where a part of the channel region ($0.3 \mu\text{m} \times 3.2 \mu\text{m}$) is indicated. The number of implanted ions in the channel was set to 96. For comparison with the ordered array, samples with random doping were also prepared by implanting P ions at intervals of 300 nm under the condition that the aiming precision was intentionally lowered to 170 nm (figure 30(b)). The number of ions was set exactly similar to that in ordered doping. The implanted samples were then lamp-annealed at a temperature of 900 °C for 3 min in a N_2 atmosphere to electrically activate the implanted ions. V_{th} measurement was carried out under the same condition as that for the initial V_{th} measurement and the difference between V_{th} before and after the SII was evaluated.

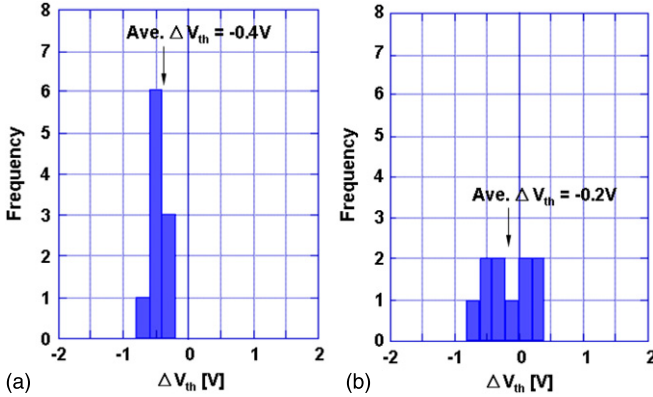


Figure 31. Histograms of V_{th} shift (ΔV_{th}) before and after SII from ten resistors. (a) Ordered dopant distribution. (b) Conventional random dopant distribution. Gaussian fitting (curve) in the ordered dopant distribution shows a standard deviation of only 0.1 V, which is three times smaller than that for the random distribution.

The V_{th} shift of our devices was derived by using standard FET equations. The V_{d} dependence of I_{d} in a device with channel length L , width W and thickness t_{SOI} in the low-bias linear region is deduced as

$$I_{\text{d}} = (Wt_{\text{SOI}}/L)\mu_{\text{n}}C_{\text{T}}(V_{\text{g}} - V_{\text{th}})V_{\text{d}}, \quad (12)$$

$$V_{\text{th}} = (1/C_{\text{T}})(Q_{\text{it}} - qN_{\text{D}} - qN_{\text{D}}^{\text{i}}) = V_{\text{th}}^{\text{i}} - qN_{\text{D}}/C_{\text{T}}. \quad (13)$$

Here, μ_{n} is the mobility, q the elementary charge, N_{D}^{i} and N_{D} the initial and implanted dopant concentrations, C_{T} the total capacitance per unit area and Q_{it} the Si/SiO₂ interface-trapped charges. V_{th} monotonically decreases as the number of implanted ions increases. We defined the difference between the V_{th} shift (ΔV_{th}) before and after SII as

$$\Delta V_{\text{th}} = V_{\text{th}} - V_{\text{th}}^{\text{i}} = -qN_{\text{D}}/C_{\text{T}}. \quad (14)$$

ΔV_{th} is directly proportional to the number of newly added dopants and hence is a good means of counting the number of added dopants. By assessing ΔV_{th} , we eliminated the fluctuations unintentionally incorporated during device fabrication processes, such as the fluctuation in initial dopant distribution, lithographical channel size and film thickness.

Figure 31 shows the histograms of the ΔV_{th} distribution obtained from 10 FETs with ordered channel doping and 10 FETs with random channel doping. The ΔV_{th} distribution of FETs with the ordered dopant array (figure 31(a)) is much narrower than that of FETs with random channel doping (figure 31(b)). The ΔV_{th} values of FETs with random implantation deviated considerably from the mean value; the fluctuation in the dopant atom position from one device to another explains this dispersion. Gaussian fitting in the ordered dopant distribution shows a standard deviation of only 0.1 V, which is three times smaller than that in the random dopant distribution. We attribute the reduction in the V_{th} fluctuation to the precise control of both dopant atom number and position. In addition, we found another pronounced difference: the average value of ΔV_{th} (-0.4 V) for the ordered dopants was two times lower than that (-0.2 V) of FETs with the random dopant distribution, even though the dopant number was the

same for both FETs. The larger negative ΔV_{th} for the ordered distribution indicates that the channel is open under a lower gate voltage. We conclude that the uniformity of the channel potential lowers the voltage required to open the channel from source to drain, thereby allowing for early turn-on in parts of the channel and resulting in a lower threshold voltage. Thus, marked improvements in device properties could be obtained for future semiconductor electronics if dopant distributions could be precisely controlled. How a similar scheme could be implemented in mass production remains an open question.

5. Direct observation of SII sites by ion-gun/STM combined system (IG/STM)

In this section, we describe the common feature of SIIr for both probing (SIMP) and modification (SII). The common feature is ‘defect cluster’ formation that results from disorder formation along the ion tracks. In section 5.1, we discuss the identity of defect clusters along ion tracks. The defect clusters are composed of displaced host atoms, vacancies and implanted atoms. They exert a great influence on material properties and device characteristics; most of these influences are usually harmful but some are occasionally useful in certain circumstances. Therefore, we need to understand in detail the identity of defect clusters and their subsequent behaviour during thermal annealing for crystal recovery.

Since the annealing behaviour of defect clusters is inevitably associated with the behaviour of point defects, we need to obtain a novel tool to observe this behaviour. For this, we developed the IG/STM [39, 40], which enabled us to directly observe ion incident sites on a nanometre scale. This approach is discussed in section 5.2.

In section 5.3, the behaviour of point defects during the annealing process of defect clusters is discussed. In sections 5.3.1 and 5.3.2, the behaviours of vacancies and Si interstitials are described based on observations using the IG/STM. In section 5.3.3, we shed light on the interaction between point defects, which result in the formation of defect complexes.

In section 5.4, we relate the results obtained by SII and *in situ* defect studies to radiation effects in devices induced by SIIr.

5.1. Identity of defect clusters formed along ion tracks

Single ions implanted into a solid at a certain acceleration energy lose energy by both elastic and inelastic collisions as they penetrate deep into the solid and finally stop at a certain depth called the ‘projected range’. The elastic collision induces knock-on atoms if the energy transfer is higher than the displacement energy of the host atoms. In Si crystals used for ULSI device technology, the knock-on atoms are Si interstitials (*Is*) and vacancies (*Vs*) are left behind. This is the origin of a defect cluster formation along ion tracks.

The behaviour of energetic ions implanted into materials is quite well known, and there exists a comprehensive database that tabulates the ion range and the range straggling as a function of the ion species, acceleration energy and target

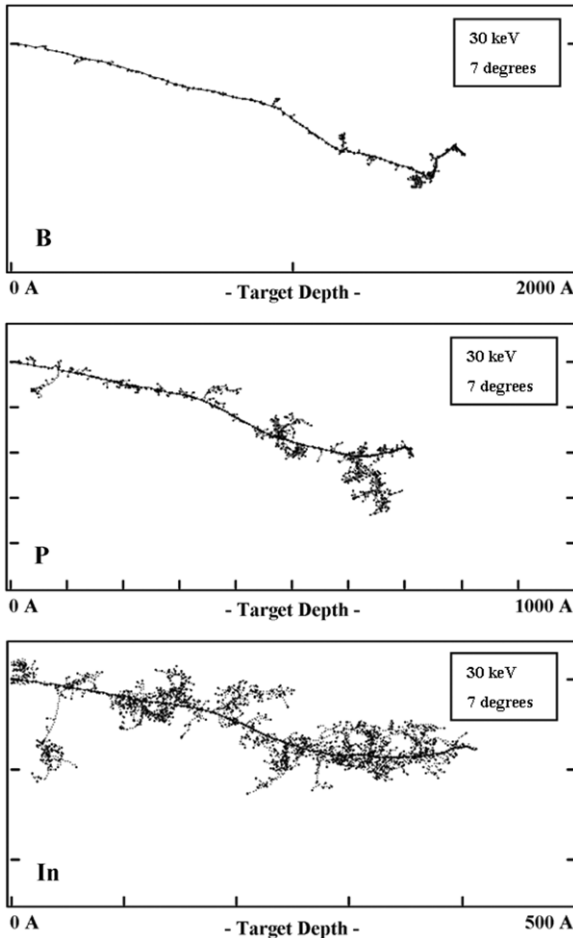


Figure 32. Examples of defect clusters formed in Si by B, P and In ions with an acceleration energy of 30 keV. These were obtained by using the SRIM code [59].

materials [60]. In addition, computer programs to calculate not only ion distributions but also defect distributions are available [61,62]. In general, a light ion with high energy loses more energy by inelastic collisions than by elastic collisions. This is the reason why RBS is a non-destructive probe of material characterization. In the case of ion implantation where ions with relatively low energy and large mass are used for material modification, the elastic collisions become dominant and many more defects are introduced. Figure 32 shows examples of defect clusters formed in Si by B, P and In ions with an acceleration energy of 30 keV. These are obtained using the SRIM code [61]. Because of the difference in the collision cross section, lighter ions penetrate deeper into a target, generating fewer defects than heavier ions.

In contrast to the comprehensive database on the as-implanted profiles of ion and defect distributions, the identity of defect clusters is hardly understood. Fortunately, the atomic-scale resolution of the STM has made it possible to visualize an individual single-ion-incident site even if ion irradiation is performed by using a conventional ion beam. In addition, from the viewpoint of applications such as nano-fabrication and nanometre-scale modification of solid surfaces, the properties and behaviour of defect clusters as a whole are more important than the atomistic identity of

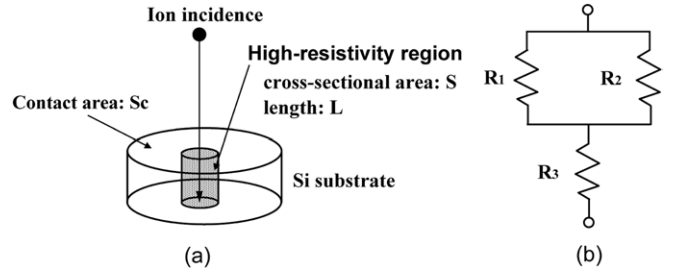


Figure 33. (a) Model of defect clusters as cylindrical high-resistivity regions. (b) Equivalent circuit of an ion-irradiated Schottky diode.

the defect clusters themselves. We will discuss how we investigated the identity and behaviour of the defect clusters as a whole by capitalizing on these above-mentioned features.

In order to estimate the ‘size’ of a defect cluster [22], we once again considered Pt/n-Si Schottky diodes (SDs) and analysed the dose dependence of the series resistance obtained from the forward I - V characteristics; we did this for the following two reasons. First, by using SDs, we can investigate the irradiation-induced defects without any thermal processes, which may alter the original properties of the defect clusters. Second, the fact that current flow is parallel to the ion tracks makes modelling simple.

In section 3 [21], we concluded that there is a very good linearity between the number of induced recombination centres, N_n , at a metal/n-Si interface and the number of He single ions. Since He ions (or Ar ions, which were used in the present work) are electrically inert in Si, the recombination centres would be V - or I -related complexes such as $V-V$, $V-O$ and $V-P$. The influence of the defect clusters on the electrical properties is due to the cooperative contribution of these point defects as a whole and appears as an increase in the electrical resistivity due to the deactivation of dopants and degradation in mobility. For the analysis to estimate the influential size of a defect cluster in terms of the resistivity, we assume that each irradiated ion induces a cylindrical high-resistivity region of cross-sectional area S and length L , as schematically shown in figure 33(a).

By solving a differential equation representing the growth rate of the high-resistivity area with respect to the ion dose, ϕ , we can derive the following relationship between the total ion dose and total high-resistivity area S_A [63].

$$S_A = S_C(1 - \exp(-\phi S)), \quad (15)$$

where S_C represents the contact area of the SD. In order to correlate the ion dose with the series resistance, we separated the Si surface layer of thickness L into two parts: the damaged region and the undamaged region. It is reasonable that the resistance values for the damaged region (R_1) and the undamaged region (R_2) are determined by the areas S_A and $S_C - S_A$, respectively. We defined the resistance R_3 as the parasitic resistance of the Si substrate and wafer back contacts. The equivalent circuit for the series resistance of an ion-irradiated SD is shown in figure 33(b).

The SDs were fabricated using a thermally oxidized n-type Si(1 0 0) wafer (ρ : 1–2 Ω cm) with a circular opening

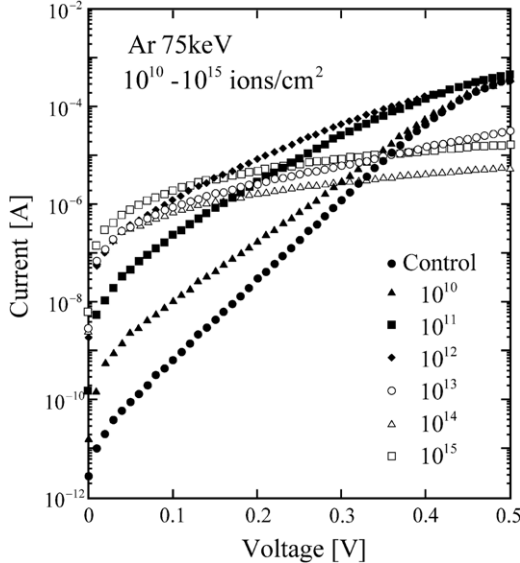


Figure 34. Forward I - V characteristics of Schottky diodes irradiated with Ar ions at 75 keV.

200 μm in diameter. Ar ions (75 keV) were implanted into the specimens at room temperature at doses ranging from 10^{10} to 10^{15} ion cm^{-2} . After some chemical treatments to clean up the implanted surfaces, Pt thin films that were 25 nm thick were deposited through a metal mask with a circular opening of 600 μm at room temperature to form SDs. It is noteworthy that no heat treatment was performed and hence the defect clusters induced by Ar irradiation remained in the SDs with larger diameters and shorter cylinder lengths L as compared with those in the case of He irradiation.

Then we measured the I - V characteristics of the irradiated Pt/n-Si SDs using HP4140B at room temperature. In order to determine the series resistance in each irradiated SD from its I - V characteristics, we performed parameter fitting, which is described in section 3 [21]. Figure 34 shows the forward I - V characteristics of SDs irradiated with Ar ions. In low-current region, the saturation current density increased markedly with the ion dose. In the high-current region, the forward current gradually decreased with an increase in the Ar ion dose. As discussed in section 3, these changes in the I - V characteristics can easily be analysed on the basis of three parameters: Schottky barrier height, recombination current density and series resistance. In the next paragraph, we particularly focus on the change in the series resistance.

Figure 35 shows the relationship between the Ar ion dose and the series resistance. It is clear that the series resistance increases abruptly by two orders of magnitude between 10^{12} and 10^{13} ion cm^{-2} . It is very interesting to note that the critical ion dose for the saturation of the series resistance (10^{13} ion cm^{-2}) is 1 or 2 orders of magnitude lower than that for the formation of continuous amorphous Si surface layers (10^{14} to 10^{15} ion cm^{-2}) for Ar and Si ions at room temperature [64]. Since a continuous amorphous layer is formed by the overlapping of the ‘amorphous core’ around the ion tracks, the much lower dose for the saturation of the series resistance implies that the high-resistivity region around an ion track is much wider than the initial ion cluster. The reason for the larger

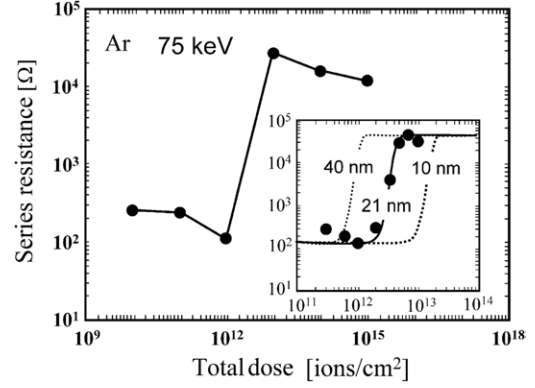


Figure 35. Change in series resistance with Ar ion dose.

influential region in the electrical properties than the region of the amorphous core is the out-diffusion of Si interstitials (I_S) and vacancies (V_S), as discussed in section 5.3.3.

Based on the experimental result on the series resistance R_s , we can estimate the size of the defect clusters as follows. Before ion irradiation ($\phi = 0$), since $R_1 = 0$, $R_s = R_2 + R_3 \equiv R_L$ (series resistance at zero dose). At the highest dose, where $S_c = S_A$, $R_2 = 0$ and $R_s = R_1 + R_3 \equiv R_H$. At an intermediate dose ϕ , R_s is given by the following equation [20]:

$$R_s = (R_H - R_L + M) / \{1 + (R_H - R_L + M) \exp(-\phi S) / M\} \\ + R_L - M, \quad (16)$$

$$M = \rho L / S_C,$$

where ρ is the resistivity of the undamaged Si substrate and R_L and R_H are the series resistances as defined above. The inset in figure 35 shows the magnified curve in the range of 3×10^{11} to 1×10^{13} ions cm^{-2} . The dose rate was maintained at 1.5×10^{10} ions $\text{cm}^{-2} \text{s}^{-1}$ throughout this dose range in order to avoid any ambiguity induced by the dose rate dependence of the residual amount of disorder. The solid line in this figure represents the best fit of equation (16) to the experimental plots with S as a parameter, assuming L to be 150 nm. This value of L is the range of that for 75 keV Ar ions in Si, as estimated from the TRIM code. The two dotted lines in the inset in figure 35 represent the theoretical curves for diameters of 10 and 40 nm. The slight difference in the diameter results in a large discrepancy with respect to the experimental plots. Thus, we can conclude that a single Ar ion induces a defect cluster with a diameter of 21 nm. The lateral vacancy distribution in terms of the full width at half-maximum was estimated to be 22 nm on an average by using the TRIM code. This coincidence is quite good.

5.2. Approach to directly observe single-ion-incident sites

In this section we describe the development of a means to characterize the dynamic aspect of single-ion-induced surface defects [39].

The modification of semiconductor surfaces by ion-beam irradiation is promising as a ‘seeding’ technique for the subsequent processing of sub-micrometre or nanometre-scale

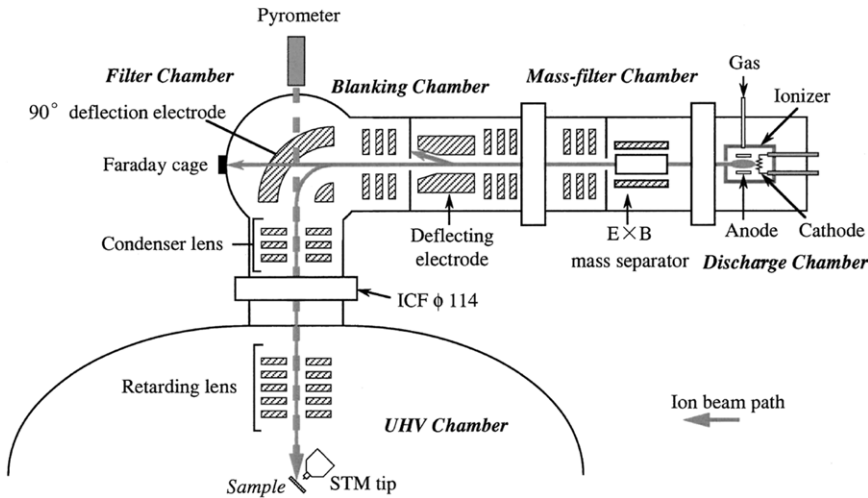


Figure 36. Schematic diagram of ion-gun/ultrahigh vacuum (UHV) high-temperature STM combined system (IG/STM).

structures ([39] and the references therein). In order to modify solid surfaces in a precise and well-controlled manner, it is important to understand the structure and/or electronic states of the modified sites and their dynamic behaviour during heat treatment. So far, several groups have investigated the microscopic aspects of defects induced by ion-beam irradiation on Si surfaces using scanning tunnelling microscopy (STM) or scanning tunnelling spectroscopy (STS) (references 8, 9, 10 in [39]). These pioneering works, however, are not direct in terms of place and time, i.e. the observations were not done *in situ* or in real time. Thus, the microscopic aspects of the dynamic behaviour of ion-irradiated sites still remain unclear. To address this issue, we built a low-energy ion-gun/ultrahigh vacuum (UHV) high-temperature STM combined system (IG/STM).

The setup of the system is schematically shown in figure 36. The ion-gun (Omegatron Ltd.) consists of four chambers and is connected to a UHV chamber equipped with a high-temperature STM unit (JEOL 4000XV). In the discharge chamber, ions are generated by introducing a source gas of up to about 0.1 Pa into a filament-type ionizer. The extracted ions are selected by an $E \times B$ mass separator in the mass-separation chamber, bent at 90° in the filter chamber and irradiated onto a sample surface located in the STM unit in the UHV chamber. The ion-incident angle is tilted at 47° with respect to the surface normal in order to minimize channelling for Si(1 1 1) surfaces. The ion acceleration voltage is controlled within the range 0–5 kV by changing the electrostatic potential of the cathode. The irradiation time is controlled with an accuracy of 0.01 s by the deflection of the ion beam in the blanking chamber.

Since the pressure in the discharge chamber is high (of the order of 0.1 Pa), it is difficult to maintain UHV conditions in the STM chamber. To solve this problem, we performed differential pumping by utilizing a four-chamber system. The chambers were compact (0.2–4 l) and connected to each other through small orifices with diameters of 1–4 mm. The filter and blanking chambers were evacuated by a magnetically floated turbo-molecular pump (TMP) (SEIKO STP301) at a pumping rate of 300 l s⁻¹ and by an ion pump (Phi Electronics Captorr

D-I) at 240 l s⁻¹, respectively. The discharge chamber was designed to be as small as possible, leading to high ionization efficiency. The bending of the ion beam in the filter chamber was efficient to reduce neutral particles. Consequently, we succeeded in maintaining the UHV chamber below 4×10^{-8} Pa before ion irradiation and at 4×10^{-7} Pa during ion irradiation. The UHV condition during ion-beam irradiation enabled us to investigate the influence of not only rare gas ions but also reactive ions such as oxygen or dopant atoms for surface modification.

The second problem was the transmission of the vibratory noise of the TMP to the STM unit. This was suppressed by elaborately installing anti-vibration components. A ‘twelve O-ring stack (JEOL)’, which consists of alternate stacks of Viton rubber rings and stainless steel plates, supported the STM unit. In addition, two rubber vibration dampers connected the TMP to the ion-gun system. Further, the whole system was located on an air damper in order to suppress external noise from the surroundings. As a result of these anti-vibration procedures, atom-resolved STM images were obtained even while the TMP was in operation. The results of the observation are shown in the next section.

5.3. Behaviour of point defects during defect annealing

5.3.1. Behaviour of vacancies [39]. Figure 37 shows typical sequential STM images of the Si(1 1 1) surface before, during and after Ar⁺ ion irradiation. The sample was maintained at 460 °C throughout the observation. Ar⁺ ions were irradiated for about 3 s at 3 kV to a dose of 1×10^{12} cm⁻², and the observation was continued in the same area. All the sequential images were obtained every 8.8 s in constant-height mode and with a sample bias of +1 V and recorded on videotapes. Before ion irradiation, as shown in figure 37(a), the surface was completely covered with well-ordered 7 × 7 dimer-adatom-stacking-fault (DAS) structures. In the next image (figure 37(b)), an Ar ion beam was switched on. Upon irradiation, the image turned white due to the incidence of positively charged Ar⁺ ions onto the STM tip. After the irradiation (figure 37(c)), small patches with diameters of

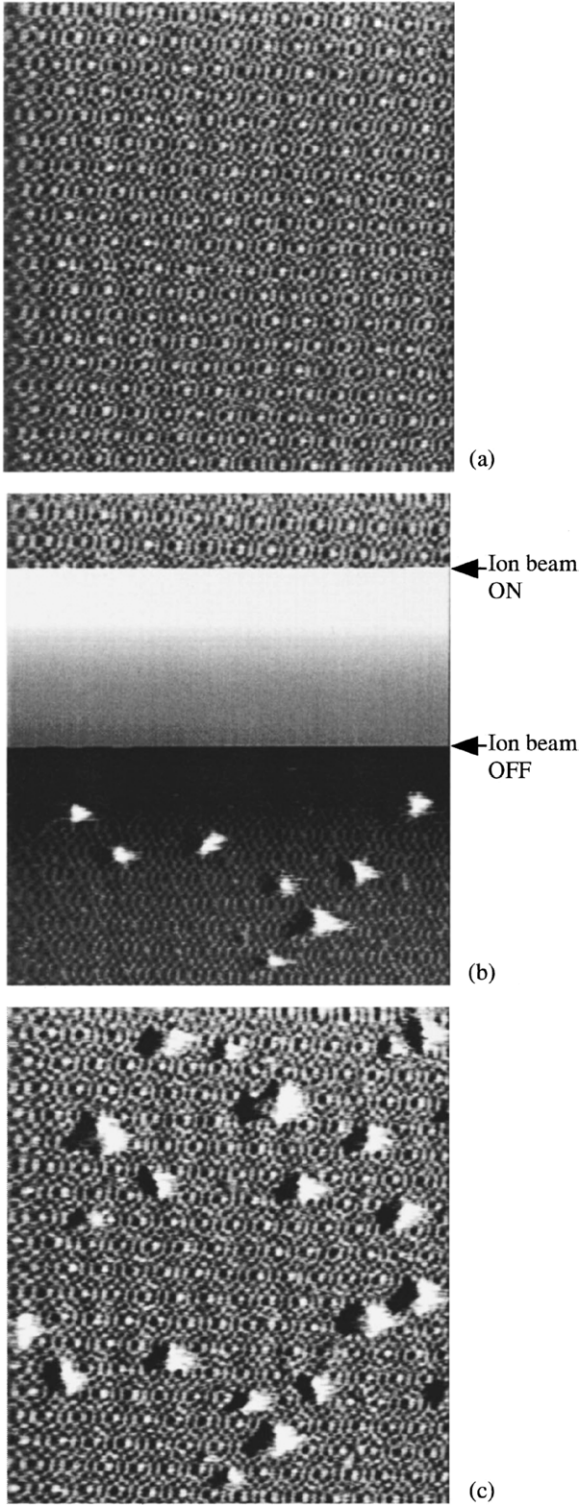


Figure 37. Typical sequential STM images ($43 \text{ nm} \times 47 \text{ nm}$) of the $\text{Si}(111)$ surface maintained at 460°C (a) before, (b) during and (c) after 3 keV Ar^+ ion irradiation to a dose of $1 \times 10^{12} \text{ cm}^{-2}$.

2–3 nm appeared on the 7×7 surface. From the relation between the scan direction and the contrast change induced by the response of the STM tip, these defects were identified to be the indents. The number of defects in figure 37(c) was almost the same as the number of incident ions, as estimated from the ion dose. It should be noted that each defect was

induced by a single Ar^+ ion. In other words, the atomic-scale resolution of the STM has made it possible to visualize a single-ion-incident site even if ion irradiation is performed by using a conventional ion beam. Therefore, in this experiment, SII was not necessary.

Figure 38 shows sequential STM images after ion irradiation. In figure 38(a), there exist three defects induced by ions in an area of $10 \text{ nm} \times 15 \text{ nm}$. The central defect shrinks in figure 38(b) and finally anneals out in figure 38(c). The lower one first expands in figure 38(b), then shrinks gradually in figures 38(c)–(e) and finally disappears in figure 38(f). The larger defect on the upper side gradually expands and does not disappear within the time range of our observation. These high-temperature STM observations reveal that the defects induced by ion irradiation show various dynamic changes. On the other hand, no changes in the defect size were observed for the samples maintained at room temperature.

Figure 39 shows sequential size changes of several defects as a function of the time elapsed after ion irradiation at 460°C . The sizes are quantitatively shown in terms of the number of missing adatoms. As seen in figure 39, drastic changes in size take place within 200 s. The disappearance of the defect is seen in 18 s after irradiation in the earliest case, whereas the most expanded defect becomes six times larger than the initial size and does not disappear for more than 1000 s. Furthermore, we find that the changes in size neither proceed at the same rate nor depend on the initial size. The various features of the changes shown in figure 39 are considered to result from the various numbers and distribution of V_s and I_s in the ion clusters. Obviously, atoms diffusing in the bulk crystal and on the surface contribute to the morphological evolution of the surfaces and compensate for the local and spontaneous atom density fluctuations around the defects.

Figure 40 shows sequential changes in the defect shape observed at 500°C . The area of each image is $25 \text{ nm} \times 21 \text{ nm}$. In the first image (figure 40(a)), five defects are visible on the well-ordered 7×7 surface. Three small defects recover within 229 s and two larger ones expand. The edges of the expanded defects gradually straighten along the dimer rows on the surface DAS structures and finally take the shape of a regular hexagon in figure 40(d). The side lengths of the small and large hexagons correspond to those of one and two 7×7 unit cells on the surface, respectively. Such transformation into the hexagonal shape is often observed in expanded defects and the hexagonal shape is stable for a long time, as shown by the defects with a size of 36 adatoms in figure 39. DAS structures are formed not only on the surface but also on the bottom of the defects, as seen in figure 40(c). This means that the bottom surface is reconstructed to form a 7×7 DAS structure as the initially deep defect clusters are ‘buried’ during crystal recovery to form a hollow that is (111) bilayer deep.

The reconstruction of the bottom surfaces to a 7×7 DAS structure in the early stage of the observation enables the quantitative measurement of the defect size, as shown in figure 39, in terms of the number of missing adatoms.

5.3.2. Behaviour of Si interstitials [40]. In this section, we report the behaviour of Si islands as a result of agglomeration of I_s induced by Ar irradiation on the $\text{Si}(111)-7 \times 7$ surface.

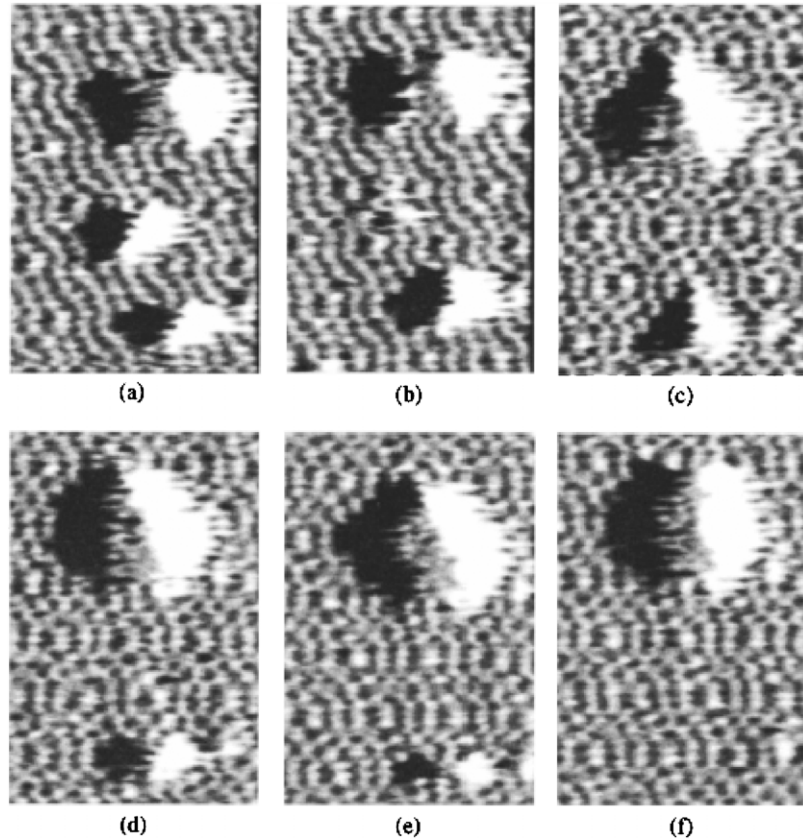


Figure 38. Sequential STM images ($10 \text{ nm} \times 15 \text{ nm}$) obtained on the Si(111) surface maintained at 460°C : (a) 26 s, (b) 35 s, (c) 44 s, (d) 70 s, (e) 105 s and (f) 123 s after 3 keV Ar⁺ ion irradiation.

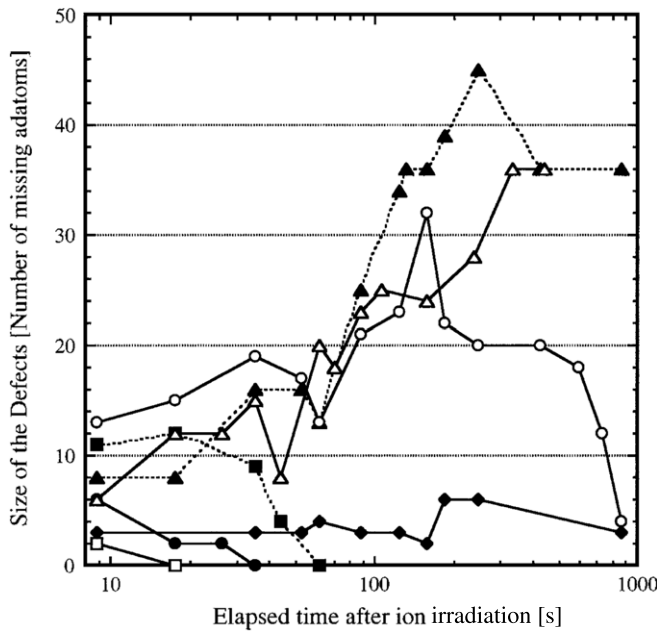


Figure 39. Size change of several defects on the Si(111) surface maintained at 460°C as a function of time elapsed after 3 keV ion irradiation. The sizes are evaluated as the number of missing adatoms.

The repeated intermittent irradiation of Ar ions for 3–5 s induces quite different features on the Si(111)-7 \times 7 surface. Ar ions were irradiated at 1 keV at a dose rate of $3 \times 10^{12} \text{ cm}^{-2} \text{ s}^{-1}$ during the STM observation. All the

sequential images were obtained every 8.8 s in the constant-height mode at a sample bias of +1 V and recorded on videotapes. Figure 41 shows successive STM images of a Si(111)-7 \times 7 surface with a domain boundary before, during and after Ar ion irradiation. For clarity, the domain boundary is delineated with a thin dotted line. Si islands are formed preferentially along the domain boundary after ion irradiation. These islands were already observed 8.8 s after ion irradiation. Although small Si islands soon disappear, larger ones survive. The critical size for survival is roughly 30 Si atoms at 500°C .

Figure 42 shows sequential STM images of Si islands on Si(111) at different ion doses. Images (c) and (d) are enlargements of (a) and (b), respectively. Si islands beyond the critical size do not disappear during annealing and grow with increasing ion dose. New Si islands are also observed along domain boundaries. These islands consist of one Si (111) bilayer and grow epitaxially on the Si substrate. DAS reconstruction is observed at the top of large islands. These features of the islands enable us to count quantitatively the number of Si atoms contained in an island by taking advantage of a 7 \times 7 DAS unit cell as a natural ‘ruler’. Some Si islands straddle domain boundaries. In these islands, domain boundaries are inherited from the Si substrate beneath and they do not change their positions.

Figure 43 shows the total area of Si islands in terms of the number of Si atoms as a function of the Ar ion dose. As the ion dose increases, the shape of the islands becomes blurred and the estimation of the area becomes more difficult.

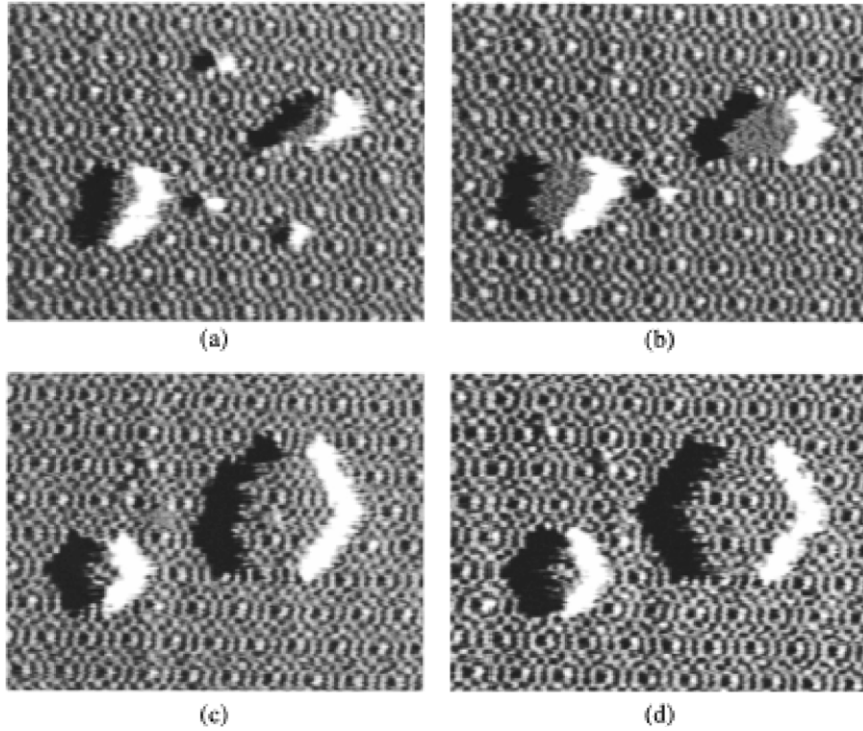


Figure 40. Characteristic successive changes in the defect shape obtained at 500 °C on the Si(111) surface irradiated with 3 keV Ar⁺ ions. The size of the image is 25 nm × 21 nm. The time elapsed after ion irradiation is 18 s in (a), 132 s in (b), 229 s in (c) and 332 s in (d).

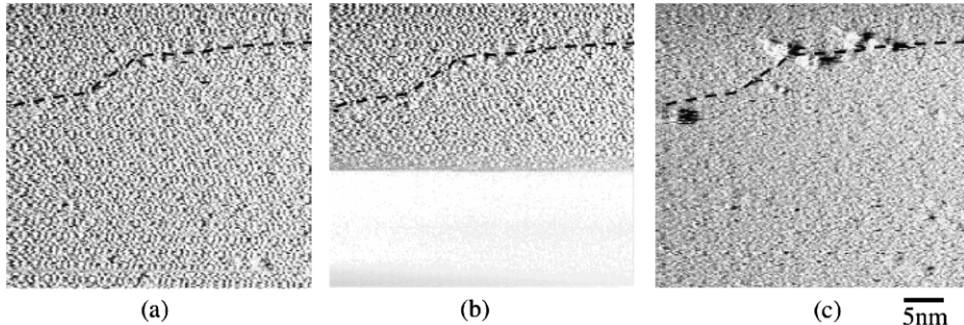


Figure 41. Successive STM images of the Si(111)-7 × 7 surface with a domain boundary maintained at 500 °C (a) 8.8 s before, (b) during and (c) 8.8 s after 1 keV Ar ion irradiation at a dose of $7 \times 10^{12} \text{ cm}^{-2}$. The dashed lines show domain boundaries.

At lower doses, a linear relationship exists between the Ar ion dose and the total area of the Si islands. It is widely known that Vs and Is are introduced in bulk crystals by ion irradiation and that they diffuse during annealing. The number of Frenkel pairs formed in Si upon Ar ion incidence at 1 keV is estimated to be 20–30/Ar ion by TRIM [61] and they distribute within 2 nm from the surface because of the rather short projected range of 1 keV Ar ions. The majority of Frenkel pairs are annihilated by direct recombination of Is with Vs. On the other hand, it is estimated from the gradient in figure 43 that one Ar ion yields about four Si Is. This means that at most, 13–20% of the Si interstitials survive from the direct recombination and contribute to the formation of Si islands.

As for the mechanism of the formation of Si islands, there are two possibilities. One is the immediate out-diffusion of the surviving Si Is through the DAS reconstructed layer and the subsequent surface migration until they settle down at

domain boundaries. The other is the lateral diffusion of Si Is beneath the 7 × 7 DAS layer and the subsequent out-diffusion preferentially through domain boundaries. We believe that the former is more probable for the following reason. It is known that Is induced in bulk Si by ion irradiation diffuse very fast [38]. These Si Is reach the surface in a very short time because their original distribution is shallow. In this connection, Kohler et al. found by an STM study on Si(111)-7 × 7 at a temperature of around 330 °C that two-dimensional Si islands preferentially nucleate at domain boundaries during the molecular beam epitaxial growth (MBE) of silicon [65].

These results show that Si islands are formed along a domain boundary on Si(111) regardless of the sources of the Si atoms supplied during annealing. There is a possibility that Si atoms sputtered from the Si surface upon ion incidence may return to the surface and contribute to the formation of Si islands. However, the sputtering yield under our experimental

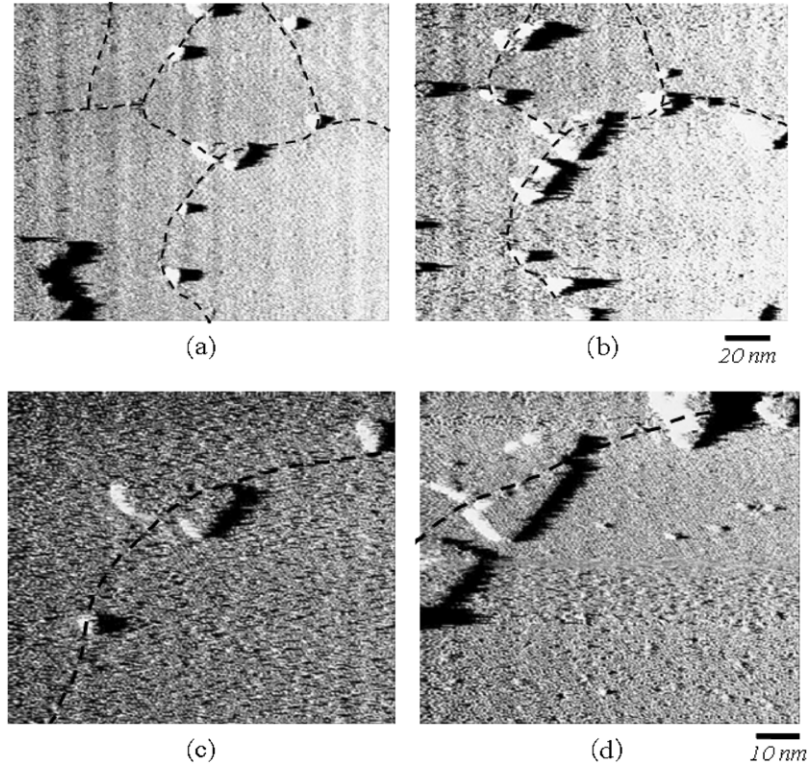


Figure 42. Si islands along domain boundaries after (a) $4 \times 10^{13} \text{ cm}^{-2}$ and (b) $1 \times 10^{14} \text{ cm}^{-2}$ 1 keV Ar ion irradiation on Si(111) maintained at 500 °C; (c) and (d) are magnified images of (a) and (b), respectively. The dashed lines show domain boundaries.

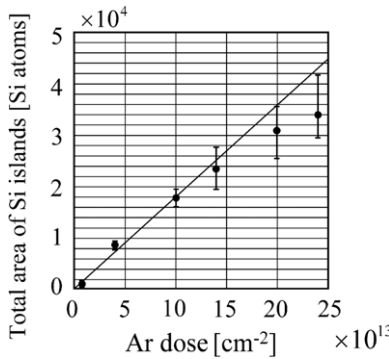


Figure 43. Correlation between Ar ion dose and the size of Si islands. (1 keV Ar, 500 °C).

conditions was estimated by TRIM to be $2.4/\text{Ar ion}$ [61]. This value is insufficient to explain the total number of Si atoms that take part in forming Si islands. In addition, it is difficult to imagine that all the sputtered Si atoms accumulate onto the surface.

It is interesting to compare the behaviour of vacancies and interstitials. Vacancies have no preferred place for ‘island’ (i.e. hollow) formation, while Si interstitials agglomerate along domain boundaries. This difference can be ascribed to the difference in the mobility of Si *Is* and *Vs* on the Si(111) surface at approximately 500 °C. *Vs* tend to cluster around each other because of lower mobility, while Si *Is* move around rapidly and find stable sites such as domain boundaries. In this context, it has been reported that Si *Is* migrate faster than *Vs* in the Si substrate [38, 66].

5.3.3. Behaviour of defect complexes [38]. In the previous sections, we revealed some features associated with single-ion incidence and the subsequent behaviours of *Vs* and *Is* in Si. *Vs* and *Is* that are induced upon ion incidence and that survive direct recombination localize along the ion tracks and subsequently diffuse outward. The lateral migration of these point defects is very important because it has a profound influence on the diffusion of the implanted dopant atoms (enhanced diffusion) [67, 68], electrical deactivation of dopant atoms and accumulation of trap levels. Obviously, this is harmful for further miniaturization of Si devices and for the integrity of device functions. Since *Vs* and *Is* are not stable at room temperature, we need to immobilize and detect them somehow. Our proposal to probe the behaviours of *Vs* and *Is* in the lateral direction is to capitalize on the advantages of our technology, i.e. the controllability of both the ion dose and incident sites. We also used deep-level transient spectroscopy (DLTS) to identify defect complexes induced by *Vs* and *Is*.

A straightforward way to investigate the lateral migration of point defects is to control the distance between incident sites of ions accurately. In this study, we introduced point defects by means of a focused Si ion beam with a beam diameter of $<0.1 \mu\text{m}$. By drawing a line-and-space pattern with an FIB and changing the separation between the lines, the effect of the migration distance of the point defects on the total number of residual defect complexes was investigated.

A Czochralski-grown (Cz) n-type Si(100) wafer with a phosphorous concentration of $1.15 \times 10^{16} \text{ cm}^{-3}$ was used as the target in this study. The oxygen and carbon concentrations in the wafer were estimated by secondary ion mass spectroscopy

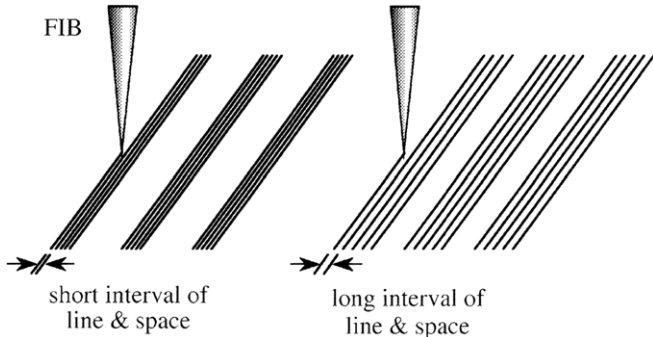


Figure 44. Schematic view of localized ion implantation using FIB. Only the separation between line-shaped implanted regions was changed by keeping the total dose constant.

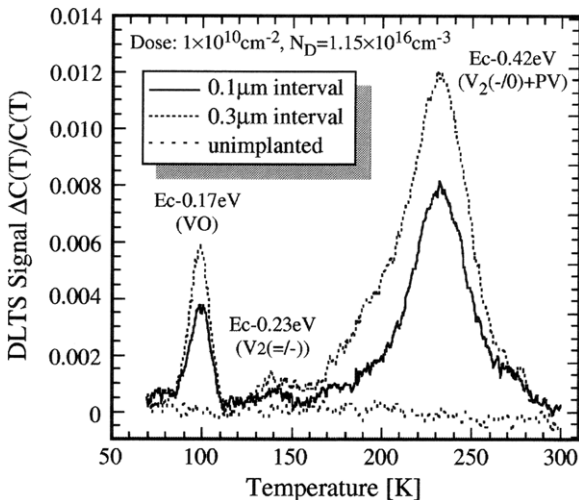


Figure 45. DLTS spectra of defects induced by FIB implantation of 60 keV Si ions to a dose of $1 \times 10^{10} \text{ cm}^{-2}$. Spectra for different separations of line-and-space patterns (0.1 and 0.3 μm) are compared.

(SIMS) as $2 \times 10^{17} \text{ cm}^{-3}$ and $<2 \times 10^{16} \text{ cm}^{-3}$, respectively. Si ions with a beam diameter of less than 0.1 μm were irradiated into the specimen at 60 keV. The Si ions were selectively irradiated into a line-and-space pattern. The average dose in the whole pattern was maintained at $1 \times 10^{10} \text{ cm}^{-2}$. Only the interval of the line-and-space patterns was varied, as shown in figure 44. After the irradiation, Pt/n-Si SDs were formed for DLTS. In order to avoid the parasitic annealing effect, the temperature of the specimen was maintained at less than 35 °C during Pt deposition. The species and concentrations of the point defects induced by the irradiation were characterized by DLTS.

Figure 45 shows two DLTS spectra obtained after the line-and-space irradiation with 0.1 and 0.3 μm intervals. Three trap levels are recognized at 0.17, 0.23 and 0.42 eV below the conduction band edge (E_c). The electron trap at E_c —0.17 eV is identified as the vacancy-oxygen centre (VO or the A centre) [69, 70]. The levels at E_c —0.23 eV and E_c —0.42 eV are attributed to doubly and singly negative charged states of di-vacancy (V_2) [71]. The level at E_c —0.42 eV is also influenced by the overlapping signal from vacancy-phosphorus

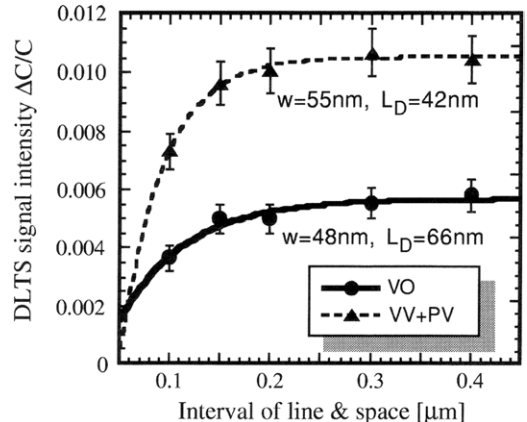


Figure 46. Correlation between number of ion-induced defects and separation of line-shaped implanted regions.

pair (PV or the E centre) [72, 73]. We should note that the height of each peak is greater at a larger line-and-space interval.

Based on the linear relationship confirmed between the DLTS signal [$\Delta C(T)/C(T)$] and the average ion dose of up to $1 \times 10^{11} \text{ cm}^{-2}$, the DLTS signal intensity can be used to monitor the relative difference in the amount of induced defect complexes. The intensity of the two clear peaks in the DLTS spectra is plotted as a function of the separation between the line-and-space irradiated regions in figure 46. The concentration of both the E_c —0.17 eV (VO) and the E_c —0.42 eV (PV + V₂) levels increases with the increase in the line-and-space interval from 0.1 to 0.2 μm and saturates at around 0.4 μm . This can be analysed as follows.

Incident ions generate a number of Vs and Is along their tracks in a target. A fraction of them recombine directly ($I + V \rightarrow \phi$), and the remainder of the Vs form stable defects through reactions with impurities and Vs themselves ($V + X \rightarrow VX$). Thus, the more the number of Is at adjacent ion tracks, the less is the number of V-type defects. In this connection, Svensson *et al* [74] explained the reason for the suppression of defect formation at a high dose rate as the migration of Is and annihilation with Vs created at the adjacent ion tracks. This means that although Vs and Is are generated at almost the same position in an initial ion cluster, since the diffusion of Is is much faster than that of Vs at room temperature [75], Is diffuse outwards from the original ion cluster much faster than Vs. In our experiment, each line-shaped irradiation region is composed of many ion clusters, and the results that the defect generation is less at a smaller separation between the line-shaped regions can also be explained by the lateral migration of Is and their subsequent interaction in the adjacent irradiated region. The out-diffusing Is interact with trap sites such as impurities, dislocations and the surface, and the number of Is decreases by reaction with these trap sites. As the distance between adjacent irradiated regions decreases, more Is that survive the reaction can reach these regions and recombine with the Vs, which still remain at the localized irradiation regions. The residual Vs react among themselves and with other impurities to form V-type defects such as V_2 , VO and PV.

Table 2. Summary of the structures of defect clusters induced in Si by ion species used in this work (calculated data by utilizing TRIM [61]).

Subject	Ions	Energy	Projected range	Lateral struggling	Number of vacancies	Quantity of interest
SIMP	He^+	2–4.5 MeV	7.3–21 μm	388–698 nm	282–326	ΔV_{th} , ΔV_{not} , ΔV_{nit} , ΔD_{it} , ΔS
SII	Si^{2+}	60 keV	85 nm	31 nm	1053	V-related defects
	P^{2+}	60 keV	83 nm	30 nm	1134	ΔV_{th}
SD	Ar^+	75 keV	84 nm	26 nm	1378	Recombination centre density
IG/STM	Ar^+	1–3 keV	3.5–6.8 nm	1.5–2.6 nm	30–83	Number of surface Vs and I_s

Note: SIMP: Single-ion microprobe, SII: Single-ion implantation, SD: Schottky diodes, IG/STM: Ion-gun/STM combined system, ΔV_{th} : threshold voltage shift, ΔV_{not} : threshold voltage shift due to trapped holes, ΔV_{nit} : threshold voltage shift due to trapped charges by the interface states, ΔD_{it} : change in interface state density and ΔS : change in the subthreshold swing.

5.4. Discussions

Since each of the works discussed in this review was performed independently so as to obtain the best results in compliance with the objectives of the individual experiments, the choice of ion species and energy is not necessarily systematic. Hence, the only way to relate the various results in a unified manner would be to discuss them in terms of defect clusters. The structures of the defect clusters induced in Si crystals by ion species are summarized in table 2. Although the structures are not very well defined, the projected range and lateral struggling values listed in the table roughly correspond to the length and the radius of a defect cluster, respectively.

Basically, high-energy light ions used as probes have extremely small collision diameters and large penetration depths. That endorses the suitability of RBS as a probe technology. However, the nonzero probability of nuclear collision of probe ions with the host atoms and the energy lost by electronic processes can induce interface defects. The ion-number dependence of the various quantities, as discussed in section 3, is a result of the non-negligible influence of the probe ions.

Near-field images of the defects at Si surfaces after Ar ion implantation are cross sections of the Ar-ion-induced defect clusters observed at the surfaces. However, the inner structures of the clusters can be revealed only by computer simulation, as shown in figure 32. What we have observed at the Si surfaces is the annealing process of the defect clusters projected onto the surfaces, namely, Vs and I_s are released from a defect cluster during annealing; some of them migrate to the surfaces and exhibit the behaviour shown in figures 37–42. Relatively low-energy Ar irradiation induces shallow defect clusters with large diameters, which facilitates near-field observation.

The structures of defect clusters formed by SII are more or less similar to the ones formed by low-energy Ar irradiation, considering the depths and the diameters of the defect clusters. Hence, we can expect similar annealing behaviours, although our concern is the behaviour of defect clusters not at the surfaces but in bulk Si. As for the formation of a periodic dopant array by SII, the ion-induced defects must first be removed as far as possible so as to obtain full electrical activation. For the DLTS observations, the lateral migration of Vs and I_s is the subject of concern. The Si ions employed

in this work induce defects and thereby introduce Vs and I_s without leaving any influence on the implanted ions themselves.

6. Conclusions

We have introduced various novel facts revealed by irradiating Si surfaces, interfaces and devices with single ions in a one-by-one manner. The revealed facts, however, have only been enumerated and more comprehensive understanding is necessary for both scientific and technological purposes.

With regard to a scientific purpose, in the near future, we aim to observe the dynamic stage of electrical activation of implanted dopant ions *in situ* by using the LMIS-IG/STM. So far, the electrical activation stage has been discussed in terms of the correlation between the overall carrier concentration and the ion dose. We intend to keep visualizing incident sites by using STM and STS, which will reveal the combined effects of crystal recovery and local change in the Fermi level position. The surfaces modified in this way will yield an electrostatic landscape at solid surfaces. This will help create various novel functions such as electron emission, catalysis, localization of electric charges, molecule immobilization and molecule recognition together with the surface topography obtained by nano-fabrication. In this connection, the combination of surface modification and the subsequent wet processing yielded various surfaces in terms of morphology, hydrophobicity, hydrophilicity and local electric charge distribution, in addition to chemically modified surfaces. For example, a nano-scale hole array formed in a glass slide has proved to be useful to accommodate a single bio-molecule in each hole and directly image single-molecule reactions [76].

With regard to a technological purpose, we are focussing on Si-CMOS technology, which has been a strong driving force that has helped maintain a worldwide Si industry growth of 8%. The ever increasing demands for higher integration have brought in an era of devices with feature sizes of tens of nanometres. Further integration, however, is facing serious roadblocks, namely, the difficulty in further size reduction due to financial and technological constraints. The Si technology community is working hard to resolve this issue and has

proposed three possible paths. These paths are ‘more Moore (MM)’, ‘more than Moore (MTM)’ and ‘beyond CMOS (BC)’ [77]. Here, ‘Moore’ implies Moore’s Law [26]. MM is the path that the community has followed thus far and will choose to keep following. MM-related issues include patterning, doping, interconnection, density, yield and cost. The so-called field of channel engineering is very important because it correlates with doping, density and yield, thereby offering great possibilities in solving some MM-related issues. Channel engineering is a general term for (1) realizing high-conductivity channels to capitalize on the stress-enhanced mobility in a nano-wire channel and the ballistic transport of carriers in an extremely short channel; (2) source (S) and drain (D) processing with a metal to form Schottky diodes with extremely shallow dopant distributions, which are induced by the ‘snowplough effect’ during silicidation [78]; (3) controlling the S&D electrostatic potential barriers for better electron injection and absorption and (4) controlling the threshold voltage by dopant atom arrangements, which are influenced by the original doping process, thermal budget and stress. Many of these issues are correlated with doping, and the controllability of both the ion number and position may be utilized to yield some solutions in the near future.

As a future issue, it is noteworthy that a solid-state quantum computer has been proposed by Kane [79]. Kane’s original proposal requires single phosphorus atoms to be placed in an array in an Si layer beneath an insulating oxide layer. However, the incorporation of the dopant array is a major problem that is yet to be overcome. In order to realize this structure, a much higher aiming precision of SII is necessary.

Acknowledgments

The author is grateful to all the coworkers who have been involved in single-ion irradiation works. The author would like to thank Professor K Yamada at Waseda University for his helpful discussions and comments. Dr K Suguro and Dr M Koyama at Toshiba Corporation, Dr M Masahara and Dr T Matukawa at the AIST, and Professors T Tanii and T Shinada and Mr T Kamioka at Waseda University helped with the preparation of figures. Dr T Chikyow at the NIMS provided useful information. Professor K Hirose at the Institute of Space and Astronautical Science, JAXA, provided useful information on the current research trends in radiation effects. Mrs A Kobayashi helped with typing the manuscript, rearranging the figures and captions and in communications with the publishers. Professor P Soukiassian at the CEA/Saclay, France, is greatly acknowledged for providing the author a chance to write this review.

This work is supported by a Grant-in-Aid for COE Research from the Ministry of Education, Sports, Science and Culture.

References

- [1] Holmes-Siedle A and Adams L 1993/2002 *Handbook of Radiation Effects* (Oxford: Oxford University Press)
- [2] Ziegler J F *et al* 1996 *IBM J. Res. Dev.* **40** 3
- [3] Dressendorfer P V 1989 *Nucl. Instrum. Methods B* **40-41** 1291
- [4] Price W E and Cross J R 1989 *Nucl. Instrum. Methods B* **40-41** 1306
- [5] Watt F and Grime G W 1987 *Principles and Applications of High-Energy Ion Microbeams* (Bristol: Hilger)
- [6] Williams J S, McCallum J C and Brown R A 1988 *Nucl. Instrum. Methods B* **30** 480
- [7] Ohdomari I, Sugimori M, Koh M, Noritake K, Ishikawa M, Shimizu H, Tanaka R, Kamiya T and Utsunomiya N 1991 *Nucl. Instrum. Methods B* **54** 71
- [8] Ohdomari I, Sugimori M, Koh M, Noritake K, Takiguchi Y and Shimizu H 1992 *Nucl. Instrum. Methods B* **72** 436
- [9] Matsukawa T, Noritake K, Koh M, Hara K, Goto M and Ohdomari I 1992 *Japan. J. Appl. Phys.* **31** 4025
- [10] Noritake K, Matsukawa T, Koh M, Hara K, Goto M and Ohdomari I 1992 *Japan. J. Appl. Phys.* **31** L771
- [11] Kamiya T, Utsunomiya N, Minehara E, Tanaka R and Ohdomari I 1992 *Nucl. Instrum. Methods B* **64** 362
- [12] Matsukawa T, Noritake K, Koh M, Hara K, Goto M and Ohdomari I 1993 *Nucl. Instrum. Methods B* **77** 239
- [13] Matsukawa T, Kishida A, Koh M, Hara K, Horita K, Goto M, Matsuda S, Kuboyama S and Ohdomari I 1994 *IEEE Electron Device Lett.* **15** 199
- [14] Koh M, Hara K, Horita K, Shigeta B, Matsukawa T, Kishida A, Tanii T, Goto M and Ohdomari I 1994 *Nucl. Instrum. Methods B* **93** 82
- [15] Koh M, Hara K, Horita K, Shigeta B, Matsukawa T, Kishida A, Tanii T, Goto M and Ohdomari I 1994 *Japan. J. Appl. Phys.* **33** L962
- [16] Matsukawa T, Kishida A, Tanii T, Koh M, Horita K, Hara K, Shigeta B, Goto M, Matsuda S, Kuboyama S and Ohdomari I 1994 *IEEE Trans. Nucl. Sci.* **41** 2071
- [17] Koh M, Horita K, Shigeta B, Matsukawa T, Kishida A, Tanii T, Mori S and Ohdomari I 1996 *Appl. Surf. Sci.* **104-105** 364
- [18] Koh M, Horita K, Shigeta B, Igarashi K, Matsukawa T, Tanii T, Mori S and Ohdomari I 1996 *Appl. Phys. Lett.* **68** 3467
- [19] Tanii T, Matsukawa T, Mori S, Koh M, Shigeta B and Ohdomari I 1996 *Japan. J. Appl. Phys.* **35** L688
- [20] Matsukawa T, Mori S, Tanii T, Arimura T, Koh M, Igarashi K, Sugimoto T and Ohdomari I 1998 *J. Appl. Phys.* **83** 3413
- [21] Koyama M, Akita Y, Cheong C, Koh M, Matsukawa T, Horita K, Shigeta B and Ohdomari I 1996 *Appl. Surf. Sci.* **104-105** 253
- [22] Koyama M, Cheong C, Yokoyama K and Ohdomari I 1997 *Japan. J. Appl. Phys.* **36** L708
- [23] Koh M, Shigeta B, Igarashi K, Matsukawa T, Tanii T, Mori S and Ohdomari I 1996 *Appl. Phys. Lett.* **68** 1552
- [24] Koh M, Igarashi K, Sugimoto T, Matsukawa T, Mori S, Arimura T and Ohdomari I 1997 *Appl. Surf. Sci.* **117-118** 171
- [25] Koh M, Igarashi K, Matsukawa T, Sawara S and Ohdomari I 1999 *J. Appl. Phys.* **85** 7814
- [26] Moore G E 1965 *Electronics Magazine* **38**(8) (Moore’s Law)
- [27] Ohdomari I 1994 *Proc. of the 1st Int. Symp. on Control of Semiconductor Interfaces (Karuizawa, Japan)* (Amsterdam: North-Holland) p 233
- [28] Matsukawa T, Fukai T, Suzuki S, Hara K, Koh M and Ohdomari I 1996 *Appl. Surf. Sci.* **117/118** 677
- [29] Matsukawa T, Shinada T, Fukai T and Ohdomari I 1998 *J. Vac. Sci. Technol.* **16** 2479
- [30] Matsukawa T, Suzuki S, Fukai T, Tanaka T and Ohdomari I 1996 *Appl. Surf. Sci.* **107** 227
- [31] Hara K, Koh M, Matsukawa T, Tanii T and Ohdomari I 1999 *Rev. Sci. Instrum.* **70** 4536
- [32] Shinada T, Kumura Y, Okabe J, Matsukawa T and Ohdomari I 1998 *J. Vac. Sci. Technol.* **16** 2489
- [33] Shinada T, Ishikawa A, Fujita M, Yamashita K and Ohdomari I 1999 *Japan. J. Appl. Phys.* **38** 3419

- [34] Shinada T, Koyama H, Hinoshita C, Imamura K and Ohdomari I 2002 *Japan. J. Appl. Phys.* **41** L287 and references therein
- [35] Shinada T, Ishikawa A, Hinoshita C, Koh M and Ohdomari I 2000 *Appl. Surf. Sci.* **162–163** 499
- [36] Shinada T, Ishikawa A, Hinoshita C, Koh M and Ohdomari I 2000 *Japan. J. Appl. Phys.* **39** L265
- [37] Shinada T, Okamoto S, Kobayashi T and Ohdomari I 2005 *Nature* **437** 1128
- [38] Matsukawa T, Yokoyama K, Sawara S and Ohdomari I 1999 *Appl. Phys. Lett.* **74** 2663
- [39] Shimada K, Ishimaru T, Yamawaki T, Uchigasaki M, Tomiki K, Matsukawa T and Ohdomari I 2001 *J. Vac. Sci. Technol. B* **19** 1989
- [40] Uchigasaki M, Tomiki K, Kamioka T, Nakayama E, Watanabe T and Ohdomari I 2005 *Japan. J. Appl. Phys.* **44** L313
- [41] Uchigasaki M, Kamioka T, Hirata T, Shimizu T, Lin F, Shinada T and Ohdomari I 2005 *Rev. Sci. Instrum.* **76** 126109-1
- [42] Traxel K 1990 *Nucl. Instrum. Methods B* **50** 177 and private communication
- [43] Breese M B H, Grime G W and Watt F 1993 *Nucl. Instrum. Methods B* **77** 301
Breese M B H, Grime G W and Watt F 1993 *Nucl. Instrum. Methods B* **77** 332
- [44] Angell D, Marsh B B, Cue N and Miao J-W 1989 *Nucl. Instrum. Methods B* **44** 172
- [45] Nicollian E H and Brews J R 1982 *MOS Phys. Technol.* (New York: Wiley) p 549
- [46] McWhorter P J and Winokur P S 1986 *Appl. Phys. Lett.* **48** 133
- [47] Lenahan P M and Dressendorfer P V 1984 *J. Appl. Phys.* **55** 3495
- [48] Gesch H, Leburton J P and Dorda G E 1982 *IEEE Trans. Electron. Devices* **ED-29** 913
- [49] Ma T P, Scoggan G A and Leone R 1975 *Appl. Phys. Lett.* **27** 61
- [50] Scoggan G A and Ma T P 1977 *J. Appl. Phys.* **48** 294
- [51] Ohdomari I, Kuan T S and Tu K N 1979 *J. Appl. Phys.* **50** 7020
- [52] Natori K 1989 *Nikkei Microdevices* No 8 p 108 (in Japanese)
- [53] Natori K 1991 *Bull. Phys. Soc. Japan* **46** 352 (in Japanese)
- [54] Gamo K, Ukegawa T, Inomoto Y, Ochiai Y and Namba S 1981 *J. Vac. Sci. Technol.* **19** 1182
- [55] Ishitani T, Umemura K, Hosoki S, Takayama S and Tamura H 1984 *J. Vac. Sci. Technol. A* **2** 1365
- [56] Clark W M Jr, Seliger R L, Utlaut M W, Bell A E, Swanson L W, Schwind G A and Jergennson J B 1987 *J. Vac. Sci. Technol. A* **5** 197
- [57] Ferron J, Alonso E V, Baragiola R A and Oliva-Florio A 1981 *J. Phys. D: Appl. Phys.* **14** 1707
- [58] Shinada T, Kobayashi T, Nakayama H, Kurosawa T and Ohdomari I 2006 A reliable method for detecting single-ion incidence *Absract of 15th Int. Conf. on Ion Beam Modification of Materials (Taormina, Italy, 18–22 September 2006)*
- [59] Hiramoto T, Yasuda Y and Takamiya M 1998 *Proc. Int. Symp. Future of Integrated Electronics (Sendai, Japan)* pp 131–5
- [60] Ziegler J F, Biersack J P and Littmark U 1985 *The Stopping and Range of Ions in Solids* (Oxford: Pergamon)
- [61] Biersack J P and Ziegler J F 1982 *Nucl. Instrum. Methods* **194** 93 (Original TRIM (the Transport of Ions in Matter))
Ziegler J F (SRIM code) <http://www.SRIM.org>
- [62] Robinson M T and Torrens I M 1974 *Phys. Rev. B* **9** 5008 (MARLOWE code)
- [63] Gibbons J F 1972 *Proc. IEEE* **60** 1062
- [64] Morehead F F Jr and Crowder B L 1971 *Proc. 1st Int. Conf. on Ion Implantation (Thousand Oaks, CA, USA)* ed L T Chadderton and F H Eisen (New York: Gordon and Breach) p 25
- [65] Kohler U, Demuth J E and Hamers R J 1989 *J. Vac. Sci. Technol. A* **7** 2860
- [66] Dunham S T, Gencer A H and Chakravarthi S 1999 *IEICE Trans. Electron. E* **82C** 800
- [67] Ohdomari I 1972 *PhD Thesis* (in Japanese)
- [68] Chao H S, Crowder S W, Griffin P B and Plummer J D 1996 *J. Appl. Phys.* **79** 2352
- [69] Watkins G D and Corbett J W 1961 *Phys. Rev.* **121** 1001
- [70] Corbett J W, Watkins G D, Cherenko R M and McDonald R S 1961 *Phys. Rev.* **121** 1015
- [71] Evwaraye A O and Sun E 1976 *J. Appl. Phys.* **47** 3776
- [72] Brotherton S D and Bradley P 1982 *J. Appl. Phys.* **53** 5720
- [73] Kimerling L C, DeAngelis H M and Diebold J W 1975 *Solid State Commun.* **16** 171
- [74] Svensson B G, Jagadish C and Williams J S 1993 *Phys. Rev. Lett.* **71** 1860
- [75] Oehrlein G S, Krafcsik I, Lindström J L, Jaworowski A E and Corbett J W 1983 *J. Appl. Phys.* **54** 179
- [76] Tanii T, Hosaka T, Miyake T, Kanari Y, Zhang G-J, Funatsu T and Ohdomari I 2005 *Japan. J. Appl. Phys.* **44** 5851
- [77] <http://www.itrs.net/Links/2005ITRS/ExecSum2005.pdf>
- [78] Ohdomari I, Tu K N, Suguro K, Akiyama M, Kimura I and Yoneda K 1981 *Appl. Phys. Lett.* **38** 1015
Ohdomari I, Suguro K, Akiyama M, Kimura I and Yoneda K 1982 *Thin Solid Films* **89** 349
- [79] Kane B E 1998 *Nature* **393** 133